Electrically Small Microstrip Antennas Targeting Miniaturized Satellites: the CubeSat Paradigm

Constantine Kakoyiannis and Philip Constantinou
Mobile Radio Communications Laboratory
School of Electrical and Computer Engineering
National Technical University of Athens
Greece

1. Introduction

A CubeSat is a type of *miniaturized satellite* used primarily by universities for space exploration and research, typically in low Earth orbits (e.g. sun-synchronous). The design protocol specifies maximum outer dimensions equal to $10 \times 10 \times 10$ cm^3, i.e., a CubeSat occupies a volume up to 1 litre (CubeSat programme, 2010). CubeSats weigh no more than 1.0 kg, whereas their electronic equipment is made of Commercial Off-The-Shelf (COTS) components. Several companies have built CubeSats, including large-satellite maker Boeing. However, the majority of development comes from academia, with a mixed record of successfully orbited Cubesats and failed missions (Wikipedia, 2010a).

Miniaturized satellites, or small satellites, are artificial orbiters of unusually low weights and small sizes, usually under 500 kg. While all such satellites can be referred to as *small satellites*, different classifications are used to categorize them based on mass (Gao et al., 2009):

1. Mini-satellite (100–500 kg)
2. Micro-satellite (10–100 kg)
3. Nano-satellite (1–10 kg)
4. Pico-satellite (0.1–1 kg)
5. Femto-satellite (0.01–0.1 kg)

CubeSats belong to the genre of *pico-satellites*; their maximum weight lies on the borderline between pico- and nano-satellites. The main reason for miniaturizing satellites is to reduce the cost of deployment: heavier satellites require larger rockets of greater cost to finance; smaller and lighter satellites require smaller and cheaper launch vehicles, and are often suitable for launch in multiples. They can also be launched "piggyback", using the excess capacity of larger launch vehicles (Wikipedia, 2010b). But small satellites are not short of technical challenges; they usually require innovative propulsion, attitude control, communication and computation systems. For instance, micro-/nano-satellites have to use electric propulsion, compressed gas, vaporizable liquids, such as butane or carbon dioxide, or other innovative propulsion systems that are simple, cheap and scalable. Micro-satellites can use radio-communication systems in the VHF, UHF, L-, S-, C- and X-band. On-board communication systems must be much smaller, and thus more up-to-date than what is used

in conventional satellites, due to space constraints. Furthermore, miniature satellites usually lack the power supply and size required for conventional bulky radio transponders. Various compact innovative communication solutions have been proposed for small satellites, such as optical (laser) transceivers, antenna arrays and satellite-to-satellite data relay. Electronics need to be rigorously tested and modified to be "space hardened", that is, resistant to the outer space environment (vacuum, microgravity, thermal extremes and radiation exposure) (Wikipedia, 2010b).

The CubeSat programme was developed through the joint efforts of research laboratories from California Polytechnic State University (Cal Poly) and Stanford University, beginning in 1999. The concept was introduced to the scientific community as an opportunity for all universities to enter the field of space science and exploration. A large group of universities, along with certain companies and organizations, participate actively in the CubeSat programme; it is estimated that 40 to 50 universities were developing CubeSats in 2004. Featuring both small size and weight, a CubeSat can be built *and* launched for an estimated total of $65,000–80,000 (per fiscal year 2004 values). The standard $10 \times 10 \times 10$ cm^3 basic CubeSat is often called a "1U" CubeSat, meaning *one unit*. CubeSats are roughly scalable in 1U increments and larger. The four basic sizes are 0.5U, 1U, 2U and 3U. The number corresponds to the length of the CubeSat in decimetres; width and depth are always 10 cm, or 1 dm. Orbiters such as a "2U" CubeSat ($20 \times 10 \times 10$ cm^3) and a "3U" CubeSat ($30 \times 10 \times 10$ cm^3) have been both built and launched. Since CubeSats are all 10×10 cm^2 (regardless of length) they can all be launched and deployed using a common deployment system. CubeSats are typically launched and deployed from a mechanism called a Poly-PicoSatellite Orbital Deployer (P-POD), developed and built by Cal Poly. The low cost of the CubeSat programme, compared to standard satellite missions, has formed a cost-effective independent means of getting a payload into orbit for many institutions around the world. Most CubeSats carry one or two scientific (measuring) instruments as their primary mission payload (Wikipedia, 2010a). Only few of them are equipped with a propulsion system that enables orbit correction or attitude control. One such example is the CubeSat built by the University of Illinois, which was loaded with an array of small ion thrusters.

CubeSats enable a vast array of research possibilities and applications. One of the key areas of study is *Earth remote sensing*: efforts there focus on earthquake detection through the detection of magnetic signals, study of the air-glow phenomenon in the Earth's atmosphere, cosmic dust detection and the possibility of terrestrial gamma-ray bursts originating from lightning. Another field of study, and a rather expensive one, is *biology*. For instance, the GeneSat-1 project by NASA was not cheap by CubeSat standards: total expenditure on the satellite and its experiments reached $6 million before GeneSat was launched on a Minotaur rocket. Its mission is to establish methods for studying the genetic changes in bacteria exposed to a space environment (Wikipedia, 2010a). Modern small satellites are also useful for other applications, such as telecommunications, space science, mitigation and management of disasters (floods, fire, earthquake, etc.), in-orbit technology verification, military applications, education, and training (Gao et al., 2008; 2009).

CubeSat missions started in 2003; that year 5 academic and 1 commercial CubeSat were carried into orbit. Successful launches continued in 2005 with 3 more CubeSats built by universities; 17 more satellites were carried into orbit between 2007 and 2010. But, in 2006, July saw the greatest disaster in the short history of CubeSats: with a payload of 14 satellites from 11 universities and a private company, a DNEPR-1 rocket was launched from Baikonur Cosmodrome, Kazakhstan; it was the largest planned deployment of CubeSats to date. The

rocket failed and crashed into the ground, obliterating the CubeSats and 4 other satellites aboard. The launch was lost after the engine responsible for the first stage of lift off stopped working prematurely. Thrust termination occurred at 74 seconds after lift off (Wikipedia, 2010a). An extensive (but incomplete) list of CubeSat missions can be found in (Wikipedia, 2010c). Out of the 52 past missions documented, 24 are currently active; 1 was successful but has been de-activated; 23 satellites failed; and the status of 4 others is unclear. Out of the 23 missions that failed, 17 cases were launch failures; the other 6 were successfully carried into orbit, but a malfunctioning system prevented them from becoming operational.

Since 2001, there has been a growing number of European universities that build and contribute their own pico-satellite(s) to the programme. The efforts of research groups from universities in Denmark, Germany and the UK have been particularly instrumental to the development of CubeSat technology.

2. Scope of the chapter

Modern small satellites require antennas to realize the following four fundamental functions, and CubeSats are no exception to the norm:

1. Telemetry, tracking and command (TTC),[1] which includes both uplink and downlink, at different frequencies

2. High-speed downlink for payload data, e.g., in Earth-observation missions

3. GPS/GNSS signal reception

4. Inter-satellite cross links

These functions often require several different antennas. Basic radiator configurations used are normally helices, monopoles, patches, and patch-excited cups, depending on frequency range, coverage requirements, and application (Gao et al., 2008; 2009).

Before moving on to the objectives of the Chapter, a few comments on frequency allocations are in order. Since CubeSats are mostly developed in academic research centres, it is easy to deduce that they are almost solely intended for educational and research (i.e., *non-commercial*) purposes. Therefore, there is a frequency allocation problem, because CubeSats could not occupy commercial spectrum. In Europe, certain frequency bands have been allocated for amateur satellite communication purposes. Examples of these frequencies are the 434.8–438, 1260–1270 and 2400–2450 MHz bands. In the US, although not strictly termed "amateur satellite", nine frequency bands have been allocated for space research. These bands fall in the 400–2700 MHz range. The most commonly used ones are 2025–2110 and 2200–2290 MHz. This Chapter addresses the problem of building nano-/pico-satellites from the antenna designer's point-of-view. Our objective is to describe the implementation of a *planar*, *low-cost* antenna solution for the TTC subsystem of a 1U CubeSat orbiter, operating in the 434.8–438 MHz band; this band, also known as the "70-cm" band, is often chosen by system designers due to favourable path loss characteristics. A radiator backed by a ground plane is required, so as to obtain "single-sided" directivity. These three initial specifications can be met with proper design of microstrip "patch" antennas. Patch antennas are manufactured using standard Printed Circuit Board (PCB) techniques; space-graded substrate materials must be used to satisfy the tighter mechanical and thermal constraints of space applications. A planar antenna is essentially a two-layer PCB, and thus it costs much less than a standard 4-layer or 6-layer PCB. What is more, if the designer implements a feeding network without

---

[1] Often abbreviated also as "TT&C".

any metallized holes (Vias), manufacturing costs drop even further. Nonetheless, it is a rather challenging design task to integrate a planar radiator that resonates at a wavelength $\lambda_0 = 687.3$ mm on a 100×100 mm^2 surface. Herein, λ_0 denotes the *free-space* wavelength.

The implementation of the CubeSat antenna is based on the following key assumptions. The satellite is built on a cubic conductive chassis having 10-cm sides. One of the six faces is totally used up by the antenna. Thus, the surface on which the antenna will be printed is a 100-mm square that will be occupied by the substrate in its full extent. The patch antenna must have both sides shorter than 100 mm. Moreover, it has been also assumed that the feed network of the antenna will reside either on a different face of the cube, or on the inside with the rest of the electronics, but definitely not on the same face as the antenna. In the latter case, antenna excitation is done with a protruding coaxial probe, i.e., a coaxial transmission line whose center conductor runs through the substrate. Last but not least, since this application is oriented towards *satellite communications*, it has been assumed that the microstrip antenna should have the ability to produce circularly polarized waves. A robust technique for the generation of circular polarization from patch antennas is the dual feed with signals in phase-quadrature. For this scheme to work, the shape of the microstrip patch, which determines the shape of the Surface Current Distribution (SCD), must display two perpendicular symmetry axes; otherwise, polarization will come out elliptical at best.

At the centre frequency $f_0 = 436.5$ MHz we get a free-space wavelength $\lambda_0 = 687.3$ mm. The size of a patch antenna should be at least equal to $\frac{\lambda_g}{2} \times \frac{\lambda_g}{2}$, where λ_g is the *guided* wavelength inside the cavity formed by the substrate and the two copper layers (Top and Bottom). If we had used a low-permittivity substrate with $\varepsilon_r \approx 1.0$ (e.g. Arlon FoamClad™), which is desirable for microstrip antennas, then the dimensions of the patch would be $\frac{\lambda_0}{2} \times \frac{\lambda_0}{2} = 343.6 \times 343.6$ mm^2. In that case, the antenna would require 12 times the area that is available on the satellite.

From the above introductory design notes it becomes obvious that the designer is forced to use extensive Dielectric Loading (DL) to obtain an initial degree of miniaturization. As it will be demonstrated in the following sections, DL alone is not sufficient in order to achieve the required total miniaturization. In any case, the high–ε_r material is bound to have a detrimental effect on bandwidth. To lessen this side-effect, a thick substrate has been chosen. To avoid further degradation of the radiation efficiency, the material should display low loss tangent (tan δ_e). The above issues preclude the use of a low-cost material, such as FR-4; the choices left to the designer are high-quality space-graded materials, such as PTFE, ceramic and alumina.

This Chapter is intended for serving the antenna engineering community as a concise *design guide* to a specific class of microstrip antennas, particularly *inductive-slit-loaded microstrip antennas*. However, the design approach and the electromagnetic modelling are applicable to any sort of microstrip antenna. This design guide will be useful for senior undergraduate and graduate students, research engineers, and practising antenna engineers in the field of printed/planar antennas. A basic understanding of electromagnetic theory and antennas is required.

The Chapter is organized as follows. Section 3 attempts an exhaustive review of existing literature on small-satellite-oriented antennas. Section 4 documents the design of the hybrid coupler which feeds the antenna with two equal-amplitude signals in phase-quadrature. The simulation environment is also described, along with details of the simulation setup used throughout the Chapter. Section 5 describes in detail the design procedure of the antenna and the miniaturization techniques employed. A large array of numerical results is given for this two-step design procedure. Section 6 discusses the simulation results and examines the

electrical performance of the antenna in terms of its electrical size. Finally, Section 7 concludes the Chapter with a summary of key findings and suggestions for further research.

3. Antennas for modern small satellites: Literature survey

The development of the antenna described herein can commence directly from system specifications. However, good engineering practice dictates that the relevant literature be surveyed first. After the state-of-the-art of the field has been determined, the antenna engineer can make a more educated guess on the course of action. Non-planar designs used are normally helices, monopoles, and open waveguides. Planar structures are usually patches and patch-excited cups. The choice depends on frequency range, coverage requirements, and application.

This Section aims to serve as an introduction to what is undoubtedly a fascinating and important part of the future of satellite antennas.

3.1 Wire Antennas and other non-planar structures

The literature review first revealed a number of studies oriented towards small satellites operating in the 70-cm band that are equipped with *linear* monopole or dipole antennas built with measuring tape. The tape remains folded while the satellite is not yet in orbit, and is held in place with Nylon fibres, which are secured using a short length of Nichrome wire inside the satellite. Once the satellite is in orbit, current passes through the Nichrome wire, the fibres melt and the linear antenna is released. Small satellites using this linear-antenna technique are studied in (Dabrowski, 2005; Galysh et al., 2000; Heidt et al., 2000; Hunyadi et al., 2002; LaBerteaux et al., 2007; Mizuno et al., 2005; Puig-Suari et al., 2001; Schaffner & Puig-Suari, 2002).

But this is not the only available option in terms of wire antenna elements. (Moghaddam et al., 2004) used a separated turnstile antenna (STA) to obtain saddle-shaped and hemispherical patterns for small low-earth-orbit (LEO) satellites at VHF and UHF bands. This STA is an array of four monopoles that are mounted symmetrically on the satellite and are electrically driven in phase-quadrature. The antenna is built with 55 cm–long wire elements and it resonates at 130 MHz. Dual-band operation in the UHF band is possible by exploiting the next natural odd (third-harmonic) resonance of the monopoles at 390 MHz. Gain in the UHF band was specified at 5 dBi.

Helices, despite being protruding radiators like monopoles, are also popular solutions. Quadrifilar helical antennas (QHAs) are suitable for small LEO satellites not only for their gain pattern, but also due to their low weight, size and cost. The QHA is made up of four coaxial identical elements, which are fed in phase-quadrature to produce circular polarization. (Rezaei, 2004) designed an S-band QHA for the TTC subsystem of the Small Multi-Mission Satellite that covers the Asia-Pacific region. The antenna operates at 2.26 GHz providing a 2% fractional bandwidth at VSWR $= 1.3 : 1$. If we denote the VSWR level by S, then fractional bandwidth scales by the factor $(S-1)/(2\sqrt{S})$ (Yaghjian & Best, 2005). Thus, at a level VSWR $= 2 : 1$ the bandwidth is estimated at 5.4%. Based on the author's description, the electrical size of this radiator, omitting the ground plane, was estimated at $ka = 2.11$ rad.[2] The result was anticipated, since QHAs are invariably electrically large antennas.

The G-shaped wire monopoles designed by (Yousuf et al., 2008) specifically target CubeSat missions. This rhombic structure is based on the concept of the loaded monopole, where a

---

[2] See Section 5.6 and Fig. 32 for the definition and importance of electrical size.

short monopole is loaded with two rectangular rings. Three versions were designed; two for the VHF (150 and 180 MHz) and one for the UHF band (370 MHz). Initial designs were done on infinite ground planes. Mounted this way, the achieved numerical bandwidths ranged between 32–42%. Bandwidth definition is ambiguous, since the authors used multiple system impedances. In any case, once the G-shaped monopoles where mounted on a finite wire-grid model of a CubeSat, their numerical electrical performance was severely affected, particularly that of the VHF versions. This is also to be expected: monopole antennas work fine as long as their ground plane is large enough. Below a certain limit, chassis-coupling-and-excitation considerations must be included in the design cycle. The electrical size of the VHF antennas was $(ka)_{\text{VHF}} = 1.26$ rad, whereas that of the UHF antenna was $(ka)_{\text{UHF}} = 1.41$ rad, i.e., slightly smaller than the size of the half-wavelength dipole. The ground plane was ignored in these estimations.

The size of helices can be reduced either by modifying the helical structure or by introducing dielectric loading (DL). Little design freedom is obtained by varying the pitch angle and diameter of the helix to reduce its size without destroying its performance. Moreover, the ground plane of helical antennas needs to remain large enough for good performance. However, DL strengthens the near field, increases the quality factor, and reduces the operational bandwidth of the helix. (Niow et al., 2009) proposed a well-balanced combination of a modified helical antenna and DL to reduce antenna size. The modified structure was a backfire bifilar helical antenna (BBHA), which, unlike conventional helices, does not require a ground plane. This structure is still relatively large, thus a dielectric rod was introduced around the feeding coaxial cable to reduce the size further. The dielectric rod was bound to affect antenna gain and bandwidth. Therefore, trade-offs were made between size reduction and antenna performance. All developed antennas operated at 2.6 GHz. The chosen performance metrics were broadband gain and axial ratio (AR) bandwidth. The initial (unloaded) BBHA featured a gain of 4 dBi and an AR bandwidth equal to 0.8 GHz. Its electrical size is calculated at $(ka)_{\text{ini}} = 2.22$ rad. The second BBHA was loaded with a Teflon rod. It featured a peak gain of 4 dBi and an AR bandwidth equal to 0.4 GHz. Its electrical size was reduced by 19.5% to a new value of $(ka)_{\text{Teflon}} = 1.78$ rad. The third BBHA was loaded with a Macor rod. It featured a peak gain of 3.7 dBi and an AR bandwidth equal to 0.4 GHz. Its electrical size was reduced by 24% to a new value of $(ka)_{\text{Macor}} = 1.72$ rad. Note that the electrical size of a half-wavelength dipole equals $(ka)_{\lambda/2} = 1.57$ rad.

High-frequency bands, like the X-band, provide for physically small antennas regardless of structure. (Galván & Colantonio, 2009) implemented a waveguide-based antenna for the data-downlink subsystem of the SAC-D/AQUARIUS mission, which is a LEO earth observation satellite. The radiating part is a compact choke ring antenna with reduced back-radiation. The structure consists of a segment of circular waveguide surrounded by equally spaced concentric rings ("corrugations"). Flaring of the waveguide was not allowed, in order to avoid narrowing the beam; a hemi-spherical pattern was thus obtained, according to specifications. The antenna operates at 8.2 GHz with a 5% fractional bandwidth and a gain of 7.4 dBi. The electrical size of the radiating element alone was calculated at $ka = 2.99$ rad.

This part of the literature survey is concluded with the recent study by (Nohmi et al., 2010), in which the authors implemented a solar paddle antenna for the "KUKAI" pico-satellite mission of the Kagawa University, Takamatsu, Japan. The solar paddle antenna is a bent wire radiator installed around the circumference of the solar paddle. This is a low-cost implementation, since it requires only a segment of wire and a few ferrite beads to separate the power supply line from high-frequency signals. This type of antenna simplifies the structure of the satellite,

reduces its weight and provides the necessary directivity. From the manuscript it is not particularly clear whether a single antenna or two antennas have been integrated into the periphery of the solar paddle. The radiating system operates at the VHF (145 MHz) and the UHF band (435 MHz); these two frequencies are harmonically related. Furthermore, it is clear that at the lower frequency the radiator is a $\lambda/4$–long monopole, whereas at the upper frequency the radiator is a $3\lambda/4$–long monopole.

3.2 Planar antennas for modern small satellites

One of the earliest studies on planar antennas for small satellites appeared in (Tanaka et al., 1994). To preserve area for both antenna and solar cells on a micro-satellite, the authors designed the radiating system with the solar panels attached on top of the patch antenna. The concept behind this stacked configuration is that a patch antenna, being a lossy cavity, radiates through the fringing fields appearing at its open-circuited edges. Therefore, it is irrelevant whether the solar panel is transparent to radio waves or not; the solar panel needs only to be placed in such a manner that its own power generation function as well as the radiation performance of the patch beneath it are both maintained. To this end, solar cells can occupy the whole surface of the patch and of the surrounding substrate, *except* for the region where the radiating fringing fields appear, that is, the area immediately surrounding the patch. The prototype antenna operated at 2.225 GHz with a 1.5% fractional bandwidth.

Microstrip antennas have three main feed methods: transmission line feed, optionally inset; coaxial probe feed; and aperture coupling. In (He & Arichandran, 2001), where the focus is again on micro-satellites, the authors designed a physically small, aperture-coupled patch antenna at 10.74 GHz (X-band). The antenna displays a 5.6% fractional bandwidth and a gain of 6.5 dBi (both numerical). Radiation efficiency was estimated at $n_{rad} = 0.85 = -0.7$ dB. The electrical size of the radiating element was calculated at $ka = 1.28$ rad.

In (Mathur et al., 2001) the authors describe the design of two patch antennas for the USUsat nano-satellite which is part of the ION–F constellation. The uplink antenna works at 450 MHz, and it is printed on a substrate with $\varepsilon_r = 10.2$. It also achieves a bandwidth of 7 MHz at VSWR $= 2 : 1$ (1.6%), whereas the square patch has a side length equal to 106.7 mm. To achieve circular polarization with a single feed, a coaxial probe feeds the patch along its diagonal. Its electrical size was calculated from the authors' description to be equal to $(ka)_{UHF} = 0.71$ rad. The downlink antenna resonates at 2.26 GHz and displays 4.9 dBi gain and a 17 MHz bandwidth (0.8%). It was designed on the same substrate, and it is a 20-mm square patch, thus it is estimated that $(ka)_{S-band} = 0.67$ rad. Size estimations are somewhat optimistic, since they take into account only the size of the patch, leaving out the spread of the current distribution on the ground plane.

The next study, which deals specifically with a CubeSat planar antenna, was conducted by (Fujishige et al., 2002) and (Tamamoto & Shiroma, 2002) in the framework of the CubeSat programme of the University of Hawaii. It addresses the design of a type of active antenna better known as a "grid oscillator", which is essentially a C-band active antenna array. An array of active semiconductor devices (transistors) are embedded in a grid of copper traces printed on a substrate, which serves as a DC bias distribution circuit, RF-embedding circuit and radiator. The authors in (Fujishige et al., 2002) used pHEMT devices and built a 6×6 transistor matrix on a Rogers Duroid™ substrate ($\varepsilon_r = 10.2$) at 5.85 GHz. The structure is backed by the conductive chassis of the CubeSat, which serves as a mirror to provide the necessary excess feedback for oscillation. The horizontal traces of the matrix function as DC bias lines. The vertical traces are the radiating elements, producing a vertically polarized

array that does not interact with the bias lines. The grid oscillator is actually the microwave equivalent of a laser:

1. A lossy cavity is formed by the structure and the mirror.

2. As soon as DC power is applied, oscillation is triggered by transients and/or noise; each transistor oscillates at a different frequency.

3. A non-coherent wave originates from the grid, bounces off the mirror and injection-locks the active devices; the cavity starts to reverberate.

4. Different eigenmodes compete inside the cavity, just as in a laser. Higher-order modes lose most of their power to diffraction. Single-frequency, self-locked, coherent oscillation is what remains from this process.

5. The output power from each device is combined in the far-field, making this power-combining scheme very efficient.

Unlike regular phased arrays, the spacing between the vertical traces is on the order of $\lambda_0/10$, making the grid oscillator very compact at microwave frequencies. Indeed, the outer dimensions of the grid oscillator in (Fujishige et al., 2002) were a mere 50×70 mm^2.

Several planar antennas were built to address the communication needs of European small satellite missions, such as the ESEO and SSETI-Express student missions. The size of the mini-satellite described in (Wincza et al., 2004) is $60 \times 60 \times 60$ cm^3 and it communicates at 2.025 GHz and 8.45 GHz. However, very little information is given on the topology and the electrical performance of the antenna, except an operational bandwidth of 50 MHz. Besides, the design procedure is unclear, since the microstrip patch is printed on a complex sandwiched structure to increase the bandwidth. The ESEO satellite, studied in (Idzkowski et al., 2004), communicates at 2.080 GHz and 2.260 GHz, and bears a total of six microstrip antennas for communications and telemetry. The authors cite a 7-dBi gain for this antenna system, without clarifying whether this gain holds for each antenna separately or if the antennas were grouped in two 3-element linear arrays. Their study focuses mainly on the details of the link budget of the ESEO mission.

(Muchalski et al., 2004) studied low-gain TTC antennas for the ESEO and SSETI-Express missions. The main objective of their research was the optimization of antenna placement. The authors designed a 61.4 mm square patch that was suspended 10 mm above the ground plane (air dielectric). The ground plane measured 60 cm $\times$ 70 cm and corresponded to the wall size of the spacecraft. Input impedances and radiation patterns were numerically calculated for five different simulation scenarios, which included centre-mounted, edge-mounted and corner-mounted antennas. The model corresponding to each scenario included a single antenna. The results confirmed that both $Z_{in}(j\omega)$ and the radiation pattern were severely affected by antenna placement. The centre-mounted antenna was initially designed, and it operated at 2.45 GHz. It featured a 8.2% fractional bandwidth and an electrical size $(ka)_{centre} = 2.24$ rad. When this patch was moved to either of the edges of the ground plane, the centre frequency shifted to 2.35 GHz. The operational bandwidth changed to 8.5% and the new electrical size was $(ka)_{edge} = 2.15$ rad. Finally, when the patch was moved to one of the corners of the ground plane, the centre frequency shifted to 2.275 GHz. The operational bandwidth changed to 7.9% and the new electrical size was $(ka)_{corner} = 2.08$ rad.

The antenna system of the ESEO orbiter has drawn considerable attention. An innovative, light weight, high gain antenna for the high-speed downlink of payload data of the ESEO was described by (Arnieri et al., 2004). The design is based on the shorted annular patch (SAP), which was integrated with a stacked parasitic element. The mechanical attributes

of SAPs provide for an all-metal antenna (very desirable for space applications) realized in suspended technology, leading to a compact and robust radiator. The stacked configuration provides the necessary design freedom to adjust gain and beam aperture simply by changing the distance between the two radiating elements. The nominal half-wavelength distance turns the structure essentially into a two-element end-fire linear array. The authors excited their antenna through an aperture-coupled feed, which provided circular polarization. The antenna operated at 2.425 GHz with an 8% fractional bandwidth. Peak measured gain was 12.2 dBi. The specified dimensions of the radiating parts lead to an estimated electrical size $ka = 2.50$ rad. This structure was later refined in (Arnieri et al., 2007). The updated dimensions produce a value $ka = 2.73$ rad. The stacked SAP antenna is also described in (Gao et al., 2009). Most antenna implementations target either the TTC or the payload data downlink subsystem. One of the very few studies on inter-satellite cross-link antennas picks up a topic of tremendous interest to array designers: modified Van Atta retrodirective arrays were proposed for pico-satellites operating at 10.5 GHz (Mizuno et al., 2005). The first obvious choice for cross-linking satellites is to use omnidirectional antennas. However, this choice is energy-inefficient, wasting valuable satellite resources, while at the same time it creates a satellite network that is vulnerable to eavesdropping. The second obvious alternative is to design dynamically steerable antenna arrays ("smart beamformers"). Such an implementation would tax a significant amount of resources in terms of processing power, and would introduce a complexity level that would cancel out the simple, low-cost nature of small satellites. For pico-satellite applications, a suitable alternative to dynamic beam steering is a *self-steering* retrodirective array (Mizuno et al., 2005). Retrodirective antennas are able to sense the direction of an incoming radio signal and send a reply back in the same direction. A fascinating property of retrodirective arrays is that this ability results purely from analog/RF signal processing; no digital signal processing algorithms are required at the digital baseband part of the transceiver. The topic of modified Van Atta arrays is also discussed in (Gao et al., 2009).

The S-band is also used for communication by the commercial SSTL micro-satellite built by Surrey Satellite Technology Ltd. Out of the three antennas described in (Hadj Abderrahmane et al., 2006), one is a circular patch citing a 4.9-dBi gain and main lobe beamwidth equal to 80°; this one is used for command uplink. Apart from a gain variation of 3 dB, no other details are given. Moreover, the provided radiation pattern (see Fig. 8 in (Hadj Abderrahmane et al., 2006)) corresponds to 400 MHz, not 2 GHz. Finally, the antenna depicted in Fig. 9 of (Hadj Abderrahmane et al., 2006) does not agree with the cited main-lobe beamwidth, since the circular patch seems to be equally wide with its ground plane.

(Maleszka et al., 2007) describe briefly the design of a low-profile, low-gain planar antenna for a SSETI-Express mini-satellite; the size of the satellite is $60 \times 60 \times 70$ cm^3. The antenna is mounted on a 350×350 mm^2 ground plane and operates at 2.4 GHz. Particular emphasis is placed on circular polarization generation and on maintaining an acceptable axial ratio, so that controlled degeneration to elliptical polarization is achieved.

During the initial acquisition period following the separation of the satellite from the launch vehicle, satellite stabilization has not been achieved yet; thus an omnidirectional antenna is required for communication between space and ground segment (the first established TTC link). Various low-gain antennas have been developed for TTC of small satellites at VHF, UHF and the S-band. These antennas are simple, cheap, easily fabricated, and have nearly omnidirectional or broad-beam radiation patterns, thus the satellite does not need accurate control of its attitude. One such antenna is the microstrip patch described in (Gao et al.,

2008). It uses a circular patch fed by a coaxial probe at the bottom. It is circularly polarized and operates within a tunable frequency range of 2.0–2.5 GHz, that is, inside an aggregate fractional bandwidth equal to 22%. This patch achieves a gain of 6.5 dBi at an electrical size equal to $ka = 1.99$ rad at 2.25 GHz.

Design ideas for small satellite antennas can be borrowed just as well from other segments of the antenna field, as long as the structure undergoes the necessary "space" modifications. In this context, the compact, dual-band, circularly polarized microstrip antenna (CPMA) by (Lee & Woo, 2008) is reported here. This CPMA was designed for satellite communication handsets by combining a folded patch and a plate into a stacked 3-D structure. However, the design was carried out on an electrically large ground plane, thus chassis-coupling-and-excitation considerations were not included in the design iterations. The lower band, which corresponds to the downlink, is centred around 1.61 GHz. The CPMA achieves a fractional bandwidth equal to 4.8% and a gain of 2.4 dBi. The electrical size was calculated at $(ka)_{lower} = 0.90$ rad (the ground plane was ignored in this estimation). The upper band, which corresponds to the uplink, is centred around 2.4865 GHz. The CPMA achieves a fractional bandwidth equal to 6.6% and a gain of 5.3 dBi. The electrical size was calculated at $(ka)_{upper} = 1.39$ rad.

The next study deals specifically with planar antennas targeting a CubeSat programme. (Hamrouni et al., 2009) designed and prototyped two microstrip antennas on a 1.6 mm–tall substrate. The antennas were intended for use on the first Tunisian pico-satellite ERPSat-1 and operated at 2.4 GHz (S-band). Very few details were given on the design strategy. The first prototype achieved a 2.9% fractional bandwidth with an electrical size equal to $(ka)_1 = 1.62$ rad. The second prototype achieved a 3.6% fractional bandwidth and, even though dimensions differed, its electrical size was again $(ka)_2 = 1.62$ rad.

The little space available on small satellites brings about limited capabilities for the analog/RF section. (Marrocco et al., 2010) suggested that these limitations can be overcome by exploiting the idea of "structural radiators", which has already been implemented in avionics, naval communications and hand-held terminals. This concept diverges from the use of independent sets of self-consistent radiators, and instead relies on deliberate exploitation of antenna-chassis coupling. Accordingly, radio functions are no longer fulfilled by stand-alone antennas (whips, patches, helices, etc.), while, at the same time, the satellite structure is exploited as part of the radiation mechanism. Thus, the problem of antenna integration onto small satellites can be addressed through a distributed approach, where multiple "exciter" antennas are placed all over the structure and stimulate it to produce a controllable radiation pattern. Strong coupling is expected among the exciters of the satellite, hence they must be treated as a multi-port network, i.e., designed as a whole. In their effort to demonstrate that such a system can be optimized to produce variable patterns and polarizations, the authors initially developed a tunable vertical inverted–F antenna mounted on a finite horizontal ground plane. The antenna operated at 2.3 GHz and achieved a 5.7% instantaneous fractional bandwidth. When multiple such exciters were used to design an eight-element circular array on a finite satellite body, the active reflection coefficients revealed that bandwidth was increased to 13.9% because of the configuration and coupling between the elements.

In a very recent study, (Maqsood et al., 2010) presented dual-band, circularly polarized, planar antennas for GNSS-based remote sensing applications. The authors developed a zenith and a nadir antenna that can be body mounted on-board a small UK-DMC satellite. Both antennas cover both L1 and L2 bands, centred at 1.575 GHz and 1.227 GHz respectively. In terms of compact antenna design, attention is drawn to the zenith antenna, which was initially designed as a slot-coupled stacked patch radiator. Three layers were stacked together,

with the square patch antenna on top of the upper two layers. The initial feed network comprised of three Wilkinson power dividers, which fed the bottom patch through aperture coupling. The upper patch was electromagnetically coupled to the lower patch. However, since the numerical results revealed that the radiation pattern had a strong back-lobe, the feed network was changed. Instead of aperture coupling with the bottom patch, the top patch was eventually directly connected to the feed network using vias; the bottom patch was electromagnetically coupled to the upper patch. Wilkinson dividers were replaced by a broadband three-branch coupler. The measured prototype showed a 6.3 dBi gain at the L1 and a 4.0 dBi gain at the L2 band. Calculated electrical sizes based on author data are $(ka)_{L1} = 1.82$ rad and $(ka)_{L2} = 1.42$ rad, respectively.

The literature survey is concluded with three recent review papers of great educational value, particularly for young engineers in the field (Gao et al., 2009; Wettergren et al., 2009; Zackrisson, 2007). A distinct feature of these papers is that, through an abundance of photographs depicting commercial antennas and arrays, they present state-of-the-art antennas for modern small satellites *from the perspective of the industry*. Industrial perspective is often very different from that of academia, so it could be the "rude awakening" that reveals types of antennas that have proven viable over time.

3.2.1 Antenna development at Saab Space

The first two contributions were made by Saab Space, now RUAG Aeropace Sweden. In (Wettergren et al., 2009; Zackrisson, 2007), the authors present wide coverage antennas for small satellites. Depending on frequency range, coverage requirements and application, the proposed solutions are

- Helical antennas, which are suitable for L-, S- and X-band applications
- Toroidal antennas, which are suitable for S-, Ku- and Ka-band applications
- Horns, which are suitable for Ku- and Ka-band applications
- Waveguide radiators, which are suitable for C-, X-, Ku- and Ka-band applications, and
- Patch-excited cups, which are suitable for L-, S- and X-band applications

Focusing on a few specific applications and frequency bands, it is first noted that helices and patch-excited cups are the preferred solutions for GPS/GNSS applications. The latter antenna structure is also the main choice for S-band applications, since it can implement both compact/low-gain and large/medium-gain antennas. At the X-band front, helices are used for high-speed data downlink. TTC antennas with hemispherical coverage come in two "flavours": waveguide radiators for dual-frequency operation, and patch-excited cups for single-frequency operation.

Patch-excited cups are truly versatile performers. They are light weight, robust, all-metal radiators, able to produce gains as high as 15 dBi. It can be roughly stated that their radiation pattern is designed separately from their input matching. The pattern is mainly influenced by cup diameter, rim height, and radius and height of the top-most patch. Input matching is mostly handled by adjusting the geometry of the cavity formed by the lower two patches and by changing the radial position of the feed probes. The cross-influence among these parameters is weak enough (Wettergren et al., 2009). The GPS cup described in (Zackrisson, 2007) covers both L1 and L2 bands, achieving peak gains equal to 8.5 dBi and 7.4 dBi, respectively. With a cup diameter of 160 mm, and given that rim height is about a quarter-wavelength, it is estimated that the corresponding electrical sizes are $(ka)_{L1} = 2.82$ rad and $(ka)_{L2} = 2.20$ rad. On the other hand, the S-band cup that was designed for

the LCROSS mission is a medium-gain antenna (MGA). It scored a peak gain of 12.5 dBi at 2.2 GHz, combined with an 18.2% fractional bandwidth. Nonetheless, higher gains demand larger apertures (Harrington, 1960; Skrivervik et al., 2001), thus it comes as no surprise that its electrical size is estimated in the range $4.10 < ka < 4.35$ rad.[3] Lastly, two patch-excited cups were implemented for X-band TTC applications, using different receive (RX) and transmit (TX) frequencies. The RX antenna achieves 8.9 dBi of gain, whereas the estimated electrical size of the radiating parts is $(ka)_{RX} = 2.63$ rad at 8 GHz; the choke ring has been excluded from this calculation. The TX antenna achieves 7.5 dBi of gain, whereas the estimated electrical size of the radiating parts is $(ka)_{TX} = 2.24$ rad at 8 GHz; the mounting flange has been excluded from this calculation.

3.2.2 Work described by Gao et al., IEEE Antennas Propag. Mag., 2009

The third and final contribution is by (Gao et al., 2009). The authors presented an excellent overview of the status of antennas for small satellites until the end of 2007. Work from many groups was included, albeit the focus was on the work done in this area by the University of Surrey, Surrey Satellite Technology Ltd., and the Surrey Space Centre.

The article takes off with an introduction to small satellites, describing their *modular* structure and the modules they have in common. Examples of several small satellite projects are then given, including remote-sensing micro-satellites; a student-built multiple–pico-satellite system, with a "mother-ship"–"daughter-ship" arrangement, used for communications and as a scientific test-bed; multi-university student-built nano-satellites used for a variety of purposes; and pico-satellite systems being built and used by a wide-ranging international collaboration (the CubeSat programme).

The functions and commonly used types of antennas for such small satellite systems are discussed, followed by a discussion of antenna design challenges. Due to the special environment in space and the requirements of modern satellites, there should be careful consideration of electrical, mechanical and thermal performance constraints. Yet another major consideration for antenna design is the interaction between antennas and modern small-satellite structures. The chassis of the spacecraft is a finite 3-D ground plane, which couples strongly to the radiating elements, causing electromagnetic scattering and radiation pattern blockage. These problems intensify the importance of electromagnetic simulations and measurements in an effort to obtain antenna placement for optimum performance and coverage.

The article then presents a detailed examination of the antennas used for each of the major functions associated with small satellites. Antennas for TTC applications include monopoles, PIFAs, patches, QHAs and patch-excited cups. The range of frequencies covers the VHF, UHF, S-, C- and X-bands. Antennas for high-speed payload data downlinking include S- and X-band QHAs; compact MGAs based on the SAP principle; X-band, mechanically-steered, high-gain horn antennas; deployable parabolic reflectors; S-band patch-excited cups; and UHF through S-band active antennas for CubeSat missions based on the grid oscillator concept. Antennas for satellite navigation and positioning include medium-gain patch arrays, patch-excited cups and ceramic-loaded QHAs. Inter-satellite cross links can be facilitated by high-gain patch arrays and deployable reflectors, however the most attractive option seems to be the use of low-complexity, self-steering, retrodirective arrays. In each of these areas, the requirements for the antennas are explained, followed by many examples of antennas that have been used to meet these requirements.

---

[3] The ambiguity stems from the fact that the top-most patch stands much higher than the edge of the rim.

The conclusions of the article display that this research area is flourishing, while numerous challenges remain wide open to further investigation. Innovative concepts such as "satellite-on-PCB" (PCB-Sat), where the whole satellite is built on a single PCB, as well as "satellite-on-chip" (Chip-Sat), where the satellite is built in a single chip, are paving the way for cooperative small-satellite networks with sophisticated functionalities. To satisfy the requirements of next-generation satellite communication systems, much more work is clearly pending at the antenna front.

3.3 Overview of techniques pertinent to the chapter

One of the techniques used in this Chapter is an extension of the method introduced by (Notis et al., 2004). The authors etched 40 equally long slits along the periphery of a square microstrip antenna, thus producing a meandering (ragged) outline. The ten slits on each side of the patch covered one-third of its length. (Notis et al., 2004) showed that the disturbance of the current distribution could easily bring about a 30% size reduction for a given frequency; this reduction could even reach levels up to 44%. Alternatively, a reduction in operating frequency up to 25% can be obtained, given the size of the patch.

In (Kakoyiannis & Constantinou, 2008), the authors extended this slit-loading technique by tapering the length of the slits, and thus modulating their length in the spatial domain. It was briefly shown therein that the manipulation of the spatial distribution of the slits can result in greater reduction in size and is also a way to control the input impedance $Z_{in}(j\omega)$ of the antenna. This Chapter is a detailed record of that modified miniaturization technique, which modulates slit length in order to spread the slit distribution further along the periphery of the patch.

One of the earliest studies on the use of slits in microstrip antennas was presented by (Zhang & Yang, 1998), who studied the effect of transverse slots in patches, i.e., straight slots that are perpendicular to the SCD and parallel to the phase front of the current. The authors proposed an equivalent circuit that characterizes the electrical behaviour of the slot; it is a multi-port network of inductances appearing in series with current flow. Experimental data displayed a 23% reduction in resonant frequency. This reduction can climb up to 40% if the straight slot is replaced by an "H"-shaped slot. Optimal slot positioning was also investigated: since the slot is inductive, it should be etched where the current is *maximum*, that is, at the very centreline of the patch. On the other hand, the authors did not consider the effect of slot *width*, which, in our opinion, provides a significant extra degree of freedom to further increase the *electrical length* of the patch.

A slightly more complex technique was presented in (Row et al., 2000), where four "Γ"-shaped slots are arranged in a cross order. By proper choice of slot length and inter-slot distances, a 25% reduction in f_0 can be achieved. Instead, the two wide longitudinal slits used by (Wong & Hsu, 2001) do not increase the electrical length of the patch; their placement does little to alter the SCD. However, it was experimentally proven that they augment bandwidth. The same holds for the application of "U"-shaped slots; U-slotted antennas have been investigated extensively in the open literature, and a complete design methodology is presented in (Weigand et al., 2003).

Particularly useful are techniques that achieve simultaneous size reduction (an increase in electrical length) and bandwidth enhancement. One such method unfolds in (Xiao et al., 2005), where an inset-fed patch antenna is loaded by asymmetric (alternate) peripheral slits. The slits were etched along the non-radiating edges of the patch, and achieved a 60% reduction in antenna size. At the same time, with a little help from the inset feed, two

different Transverse-Magnetic (TM) modes are excited: TM_{10} and TM_{01}. These modes are frequency-adjacent, and thus manage to double the Voltage Standing Wave Ratio (VSWR) bandwidth: these compact patch antennas displayed a fractional bandwidth close to 4%. The same research group capitalized once more on asymmetric slit loading in (Xiao et al., 2006). The new slit arrangement excites two frequency-adjacent TM_{10} modes, and manages to produce even better results in terms of size reduction and bandwidth augmentation. However, none of the above techniques is suitable for circularly polarized antennas, since they fail to preserve the required double symmetry. Therefore, in order to implement the CubeSat antenna, we decided to extend the technique presented in (Notis et al., 2004).

4. Hybrid Feed Network Design and Simulation Setup

4.1 A hybrid feed network for circular polarization

The communications antenna is used by the orbiter in both transmit (Tx) and receive (Rx) modes. Therefore, it is essential that identical radiation characteristics are maintained between modes. According to the Reciprocity Theorem (see §1.3 and §9.4 in (Stutzman & Thiele, 1998)), an antenna will maintain its properties as long as it is made out of bidirectional elements. This requirement holds not only for the body of the radiator, but for its feeding network as well; no diodes or transistors are allowed in the circuit for reciprocity to hold exactly. On the other hand, a purely passive antenna-plus-feeding-network combination will be reciprocal by definition. The hybrid coupler presented in this Section is a purely passive, bidirectional four-port microwave circuit (Bahl & Bhartia, 2003; Gustrau & Manteuffel, 2006). The model of the coupler used in simulations is shown in Fig. 1, which also indicates port numbering; ports **1** and **4** lie on the transceiver side, whereas ports **2** and **3** lie on the microstrip antenna side.
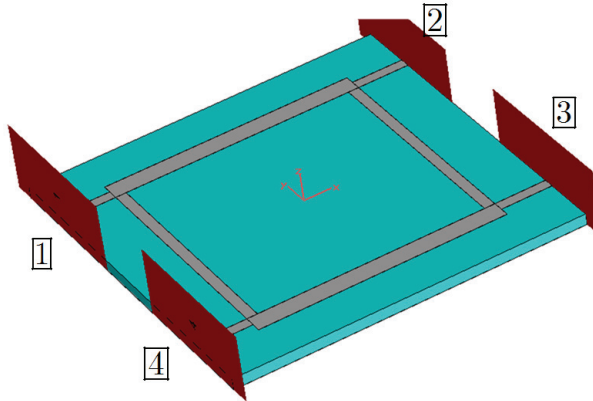
Fig. 1. Perspective view of the hybrid coupler model.

When in Rx mode, the coupler combines the signals arriving at ports **2** & **3** and produces a single output at port **4**. Port **1** is (ideally) completely decoupled from port **4**, that is, in theory we get $S_{14} \overset{\Delta}{=} 0$ and no signal power appears at port **1**. When in Tx mode, the output signal coming from the High-Power Amplifier (HPA) drives port **1**. This signal is divided into two signals in phase-quadrature ($\Delta\phi = 90°$), with each signal carrying 3 dB less power than the input signal. Thus, this circuit is essentially a power divider that introduces an excess phase

delay to one of the two branches. Port **4** is isolated from port **1**, that is, theoretically $S_{41} \overset{\Delta}{=} 0$ (Gustrau & Manteuffel, 2006).

The hybrid coupler is very well documented in the literature pertaining to microwave solid-state circuits (Bahl & Bhartia, 2003). As a result, initial predictions of the dimensions of the transmission lines that make up the coupler are readily available from theory. Before calculating any estimated values, it is important to reach a decision regarding the microwave substrate on which the coupler will be printed. The coupler is essentially composed of four $\lambda_g/4$-long microstrip lines. The designer must make sure that the guided wavelength λ_g is short enough for the whole coupler to fit on a 100×100 mm^2 area. After surveying the substrate market, the military/space-graded Rogers TMM 10i™ ceramic substrate was chosen ($\varepsilon_r = 9.80$, $\tan \delta_e = 0.0020$). Other substrates suitable for the coupler are Rogers RT/Duroid 6010LM; Rogers TMM 10; Rogers RO3010; Rogers RO3210; and Arlon AD1000. The chosen substrate height was $H = 3.2$ mm, and this is one of the advantages of TMM 10i. The thickness of the copper cladding was assumed to be 35 μm (1 oz Cu).

The design of a high-frequency circuit is an iterative procedure, even with today's advanced field solvers. The solvers decrease the number of iterations significantly, but a few iterations are always required for first-pass success on the test bench. In this context, the initial simulations revealed that the theoretical estimations for the dimensions of circuit elements needed some improvement. On the one hand, the coupler did not resonate at the desired frequency, whereas on the other hand, power was not divided equally between the two branches. To improve the design further, a parametric study was undertaken, which converged quickly to the proper circuit dimensioning that satisfies coupler specifications. The converged values are shown in Fig. 2.
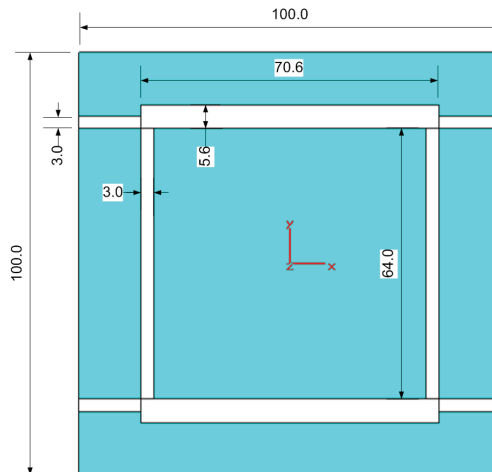
Fig. 2. Converged values of the lengths and widths of the microstrip lines of the hybrid coupler model. All dimensions are in millimetres.

4.2 Numerical results

The scattering (S-) parameters of the 90° hybrid are depicted in Fig. 3. The excitation was applied to port **1**, which is properly matched to the 50-Ω system impedance: $S_{11} < -40$ dB.

Port **4** is strongly decoupled from port **1**: $S_{41} < -30$ dB. Power impinging on port **1** is equally divided between ports **2** and **3**, since $S_{21} \approx S_{31} \approx -3$ dB. The corresponding phase diagrams (not shown here) indicate that the phase lead/lag between the signals at ports **2** & **3** is $\Delta\phi_{23} = 90.1°$.

Fig. 4 and Fig. 5 illustrate the amplitude and phase balance of the coupler, respectively. The operational bandwidth of this circuit can be defined in various ways, exactly like an antenna. So, let us choose four proper definitions:

1. The available bandwidth for a 2:1 VSWR, that is $S_{11} < -10$ dB, equals $BW_V^{hybrid} = 149$ MHz or, stated in fractional terms, $FBW_V^{hybrid} = 34\%$.

2. Instead, the frequency range where the isolation between ports **1** & **4** is better than 20 dB is much narrower: $BW_{iso20dB}^{hybrid} = 46$ MHz.

3. The operational bandwidth for a $\pm 5°$ phase balance is $BW_{\pm 5°}^{hybrid} = 148$ MHz.

4. The operational bandwidth for a ± 1 dB amplitude balance is $BW_{\pm 1dB}^{hybrid} = 140$ MHz.

Fig. 6 is an illustration of the surface current distribution on the conductive parts of the coupler; the dielectrics have been made invisible to get a clear view of the currents. Current amplitude is shown as concurrent maximum values at every point along the circuit. Of course, concurrent maxima are physically impossible because of phase shifting across the circuit; this is just a graphical tool that helps the designer identify "hot" and "cold" areas. From this rough thermograph it is obvious that power entering the circuit at port **1** is equally divided between ports **2** & **3**, whereas almost no power exits from port **4**.
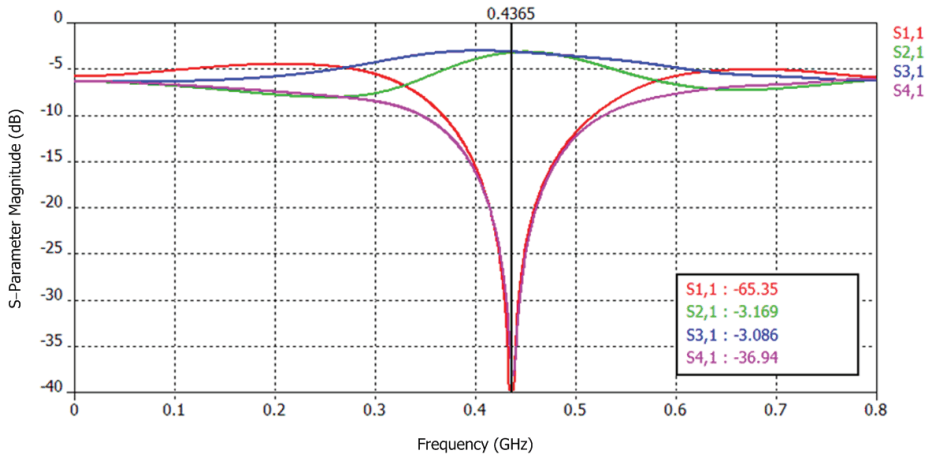
Fig. 3. Magnitudes of the S-parameters of the converged hybrid model. These parameters were obtained by exciting port **1** and terminating all other ports at the system impedance.

4.3 Field solver and generic simulation setup

All microwave systems were designed and simulated in a Transient Solver (TS) that is part of the CST Microwave Studio™ full-wave electromagnetic suite. The TS applies the Finite Integration Technique (FIT) in the time domain to reformulate Maxwell's integral equations
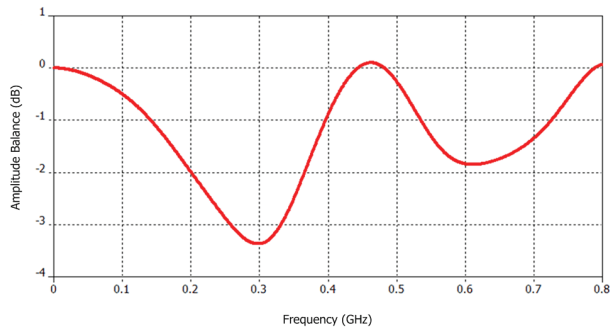
Fig. 4. Amplitude balance variation (in dB) between ports **2** & **3**. Amplitude imbalance less than ±1 dB is maintained for a 140-MHz bandwidth.
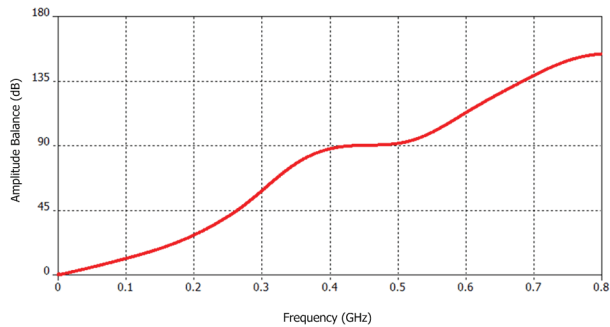

Fig. 5. Phase balance variation (in degrees) between ports **2** & **3**. Phase imbalance less than ±5° is maintained for a 148-MHz bandwidth.
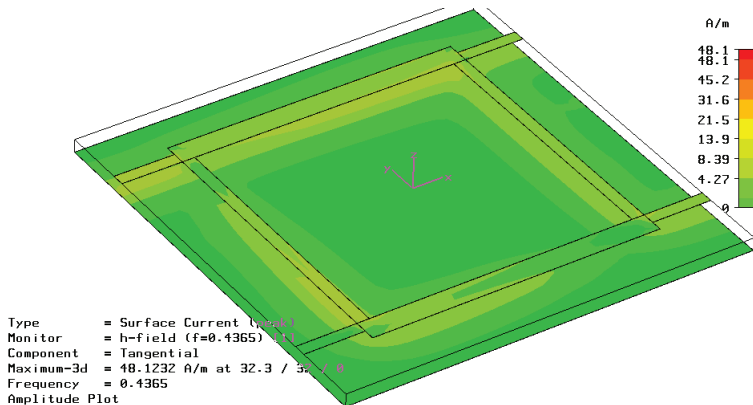

Fig. 6. Concurrent maximum values of the surface current distributed along the coupler. Note the absence of current flowing out of port **4**.

into the so-called "Maxwell Grid Equations" (Gustrau & Manteuffel, 2006; Munteanu et al., 2010; Vasylchenko et al., 2007a; Weiland et al., 2008). By applying Yee's spatial discretization

scheme and Courant's maximum stable time-step, FIT results in the same set of equations as the Finite-Difference Time-Domain (FDTD) technique (Gustrau & Manteuffel, 2006). The TS calculates the broadband behaviour of electromagnetic (EM) devices in a single simulation run, with an arbitrarily fine frequency resolution, thus without missing any resonance peaks (Vasylchenko et al., 2007a).

Time-domain solvers are particularly suitable for designing wideband antennas and passive microwave systems such as waveguide components, filters, couplers and connectors. For *active* microwave design, co-simulation is required between the EM solver and a non-linear circuit simulator, such as Agilent Advanced Design System™ or APLAC™. TSs like CST MWS can easily handle exotic materials, such as frequency-dependent (dispersive) and ferri/ferro-magnetic materials. The ability to naturally include such difficult materials in models is one of the main strengths of TSs over FEM- and MoM-based solvers, although the two latter have recently improved their material-handling capabilities (Vasylchenko et al., 2007b).

A spatially non-uniform (adaptive) hexahedral mesh discretized the objects and the solvable space in between. The mesh was refined four-fold near the edges of Perfect Electric Conductor (PEC) objects and inside the substrate to capture the large gradients of the E-field. Tetrahedral meshing is possible through Floquet modes only when FIT is applied in the frequency domain, in which case the technique results in the Finite Element Method (FEM). Nevertheless, the FIT engine used here employs the Perfect Boundary Approximation (PBA) technique (Munteanu et al., 2010; Weiland et al., 2008), and therefore the hexahedral mesh did not result in any object staircasing whatsoever.

A wideband Gaussian pulse excited the structures; its spectral content ranged from DC to 0.8 GHz. The simulator stopped when the initial system energy decayed by 50 dB. This was a good trade-off between simulation speed and truncation error in the FFT engine that translates the results from the time- to the frequency-domain. It is also a good trade-off for the near-to-far-field transformation that produces the far-field pattern of an antenna out of the fields calculated in the near-field. The maximum cell size at the maximum frequency f_{max} (smallest wavelength λ_{min}) was set to a small fraction of λ_{min}. The solvable space was terminated at an adequate number of Bérenger Perfectly Matched Layers (PML) (Bérenger, 1994), which had a normal (broadside) reflectivity of -80 dB. The distance of every object from the boundary of the solvable space was set equal to $\lambda_c/8 = 300/(8 \times 0.4)$ mm $= 94$ mm, unless otherwise noted.

Whenever a model featured topological symmetry and satisfied the appropriate boundary conditions for the electric/magnetic tangential components and the magnetic/electric flow, an electric/magnetic wall was placed across the plane of symmetry. This boundary condition reduced the computational burden significantly without loss of accuracy, because only a fraction of the structure needed solving. Complexity depends upon the level of detail exhibited by the objects comprising the model and the electrical size of the solvable space.

All structures that were modelled as part of this Chapter were fully parametrised. The key concept here is that, if the objects in a model are defined with parameters instead of numbers, then the designer benefits from parametric studies and optimization. In a sense, parametrisation creates "inflatable" models—like an accordion—instead of fixed, "frozen" models. Parametric sweeping and optimization jobs can be distributed across many "worker" computers through the corporate LAN and run in parallel. This basic form of laboratory/company distributed computing power exploitation brings about significant time savings for the design team.

4.4 Solver settings applied to the hybrid coupler

Fig. 7 depicts the spatial discretization (better known as *grid formation* or *meshing*) of the model used to design the 90° hybrid. The structure was excited in the time domain by a Gaussian pulse having spectral content in the range DC–0.8 GHz. The excitation signal along with the four output signals are shown in Fig. 8.

For efficient simulations, that is, simulations that strike a good balance between speed of execution and result accuracy, a spatially non-uniform (adaptive) grid was designed; maximum allowed grid step was equal to $\lambda_g/50$ at 0.8 GHz. No form of packaging was adopted, thus the rectangular solvable space surrounding the PCB of the coupler was terminated at a 4-layer Bérenger PML structure (Bérenger, 1994); these are *open-space* boundary conditions. This circuit is non-radiating, thus a 4-layer boundary absorber is more than adequate. However, to increase the speed of iterations, the solvable space was trimmed to half by terminating the area below the substrate at a PEC condition, i.e., $\mathbf{E}_t \equiv 0$. This approximation is valid because, when the coupler is studied in solitude, it is a non-radiating system (at least intentionally). Therefore, it is safe to assume that the ground plane of the PCB extends to infinity—this is precisely the computational effect of the electric boundary condition. The complexity of the model was $60 \times 79 \times 14 = 66,360$ Yee cells.
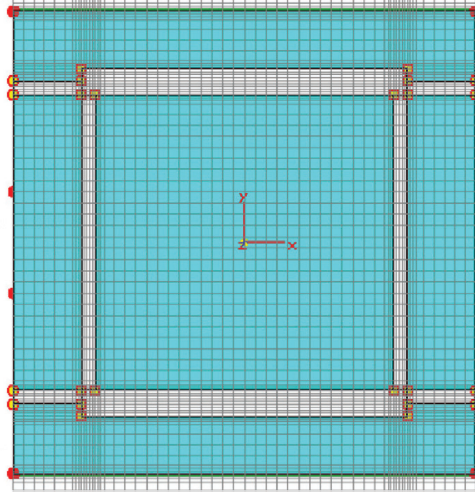
Fig. 7. The grid on which the electromagnetic problem was solved displayed a variable step ranging from 0.6 mm to 2.4 mm. Maximum grid step corresponds to $\lambda_g/50$ (or $\lambda_0/156$) at the maximum frequency $f_{\max} = 0.8$ GHz.

5. Inductive-slit-loaded Microstrip Antenna design

5.1 Antenna design considerations

Examples of microwave substrates suitable for the antenna are Rogers RT/Duroid™ 6006 and Rogers RO3006™. Both present a dielectric strength $\varepsilon_r = 6.15$, and approximately the same loss tangent; the former displays $\tan\delta_e = 0.0019$, whereas $\tan\delta_e = 0.0020$ for the latter. However, production heights differ: Duroid 6006 can be purchased laminated with a maximum height $H_{\max}^{6006} = 2.54$ mm$= 100$ mil, whereas RO3006 is sold at a maximum height
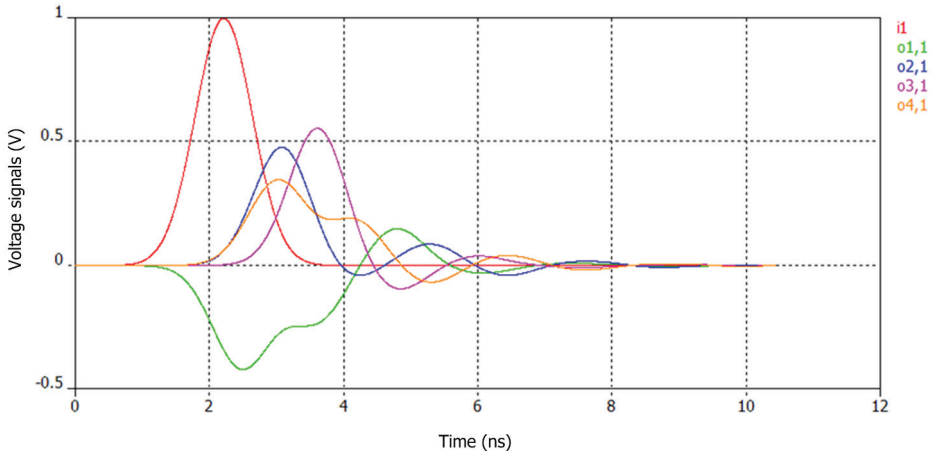
Fig. 8. Voltage signals, in the time domain, being input ("**i1**") and output ("**ox,1**", where $x \in \{1, 2, 3, 4\}$) from the ports of the hybrid coupler. System stored energy decayed to the point of terminating the execution after 10.5 ns of simulation time.

$H_{\max}^{3006} = 1.27$ mm= 50 mil. In any case, the height chosen for the CubeSat antenna substrate was equal to

$$H_{\text{patch}} = 6.4 \text{ mm} = 252 \text{ mil} \tag{1}$$

and thus bonding of several single-side-laminated substrates with prepregs is required.

The initial design stages of the antenna started out on the assumption that the same dielectric material used for the coupler would also be used for the patch antenna (Rogers TMM 10i™, ε_r = 9.80, $H = 3.2$ mm). On the TMM 10i the antenna resonated at 440 MHz for a square patch length $L_{\text{ini}} = 108.3$ mm. With a rough frequency scaling, it was estimated that the antenna would resonate at $f_0 = 436.5$ MHz for a length $L'_{\text{ini}} = 109.2$ mm. After scaling the dielectric constants, it was estimated that an antenna built on Duroid 6006 or RO3006 would have a resonant length

$$L''_{\text{ini}} = L'_{\text{ini}} \sqrt{\frac{9.80}{6.15}} = 137.8 \text{ mm}. \tag{2}$$

In theory, the resonant length of a microstrip patch antenna that corresponds to the considered parameters equals

$$L_{\text{res}}^{\text{theory}} = 0.49 \frac{\lambda_0}{\sqrt{\varepsilon_r}} = 135.8 \text{ mm}. \tag{3}$$

The deviation between the results in (2) and (3) is a mere 1.5%.

From the handy analysis unfolding in Chapter 5 of (Stutzman & Thiele, 1998) the following estimation on the real part of the input impedance of the patch can be extracted,

$$R_{\text{in}} \stackrel{\Delta}{=} Z_A = 90 \left(\frac{\varepsilon_r^2}{\varepsilon_r - 1} \right) \left(\frac{L_{\text{patch}}}{W_{\text{patch}}} \right)^2. \tag{4}$$

Substituting $\varepsilon_r = 9.80$ and $L_{\text{patch}} = W_{\text{patch}}$, we obtain

$$R_{\text{in}} \stackrel{\Delta}{=} Z_A = 90 \frac{(9.80)^2}{9.80 - 1} \; \Omega = 982 \; \Omega. \tag{5}$$

This uselessly high resistance is a side-effect of the high ε_r . This value can be reduced down to 50 Ω by setting

$$\frac{L'_{\text{patch}}}{W'_{\text{patch}}} = \frac{1}{4.43}. \tag{6}$$

Because of the severe space constraints on the spacecraft, we cannot afford to design a rectangular patch; the initial study indicated clearly that only a square patch can fit in the allocated area. All of the above, combined with the fact that the high ε_r threatens to eliminate the minimal bandwidth of the patch antenna, led us to the choice of the lower $\varepsilon_r = 6.15$. Thus, the theoretical estimation for the input resistance of the antenna now becomes

$$R_{\text{in}} = 90 \left(\frac{\varepsilon_r^2}{\varepsilon_r - 1} \right) \left(\frac{L_{\text{patch}}}{W_{\text{patch}}} \right)^2 = 90 \frac{(6.15)^2}{6.15 - 1} \, \Omega = 661 \, \Omega. \tag{7}$$

By extending the microstrip feed line inside the patch by a proper length Δx_i the *inset feed* technique is employed; the modified input resistance becomes (Stutzman & Thiele, 1998)

$$R_{\text{inset}} = R_{\text{in}} \cos^2 \left(\pi \frac{\Delta x_i}{L} \right). \tag{8}$$

Solving for $\Delta x_i / L$, which is the *fractional insertion depth*, we get

$$\frac{\Delta x_i}{L} = \frac{1}{\pi} \cos^{-1} \left(\sqrt{\frac{R_{\text{inset}}}{R_{\text{in}}}} \right). \tag{9}$$

Substituting $R_{\text{in}} = 661 \, \Omega$ and $R_{\text{inset}} = 50 \, \Omega$ we obtain the following insertion depth

$$\frac{\Delta x_i}{L} = \frac{1}{\pi} \cos^{-1} \left(\sqrt{\frac{50}{661}} \right) = 0.411. \tag{10}$$

The result in (10) means that the inset feed has to penetrate half-way along the surface of the patch; to avoid this, we used a quarter-wavelength transformer ($\lambda_g/4$–Xformer). By trading off *transformer impedance* for a mechanically robust *copper trace width*, we chose the width $W_{\text{quarter}} = 1.0$ mm, which gives a characteristic impedance $Z_{\text{quarter}} = 117.5 \, \Omega$. The length of the transformer equals $L_{\text{quarter}} = 87.0$ mm, whereas the resistance that can be matched to 50 Ω is

$$Z_x = \frac{Z_{\text{quarter}}^2}{50} \, \Omega = 276 \, \Omega. \tag{11}$$

Now the initial estimation for the depth of the inset feed can be derived,

$$\left(\frac{\Delta x_i}{L} \right)_{\text{quarter}} = \frac{1}{\pi} \cos^{-1} \left(\sqrt{\frac{50}{276}} \right) = 0.360. \tag{12}$$

However, this effort did not produce any significant reduction in inset depth; the reason is the slope of the curve shown in Fig. 9.

The 2:1 VSWR bandwidth is approximately estimated by equation (13) for $H \ll \lambda_0$ (Stutzman & Thiele, 1998)

$$\text{FBW}_V = 3.77 \left(\frac{\varepsilon_r - 1}{\varepsilon_r^2} \right) \left(\frac{W_{\text{patch}}}{L_{\text{patch}}} \right) \left(\frac{H}{\lambda_0} \right). \tag{13}$$
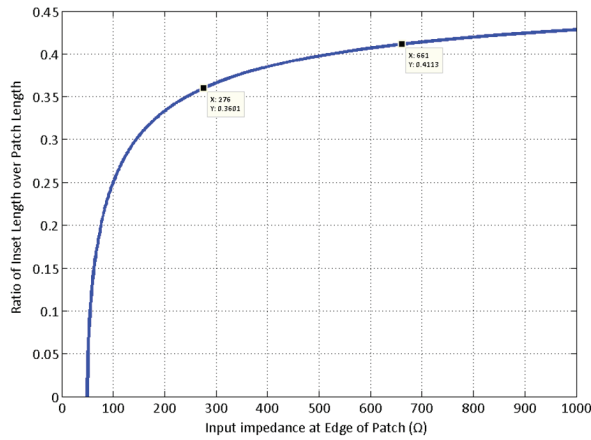
Fig. 9. Variation in required fractional inset depth as a function of the impedance seen at the edge of the patch.

Applying (13) for the parameters of this design gives the following fractional VSWR bandwidth,

$$\text{FBW}_\text{V} = 3.77 \left[\frac{6.15 - 1}{(6.15)^2} \right] \left(\frac{6.4}{687.3} \right) = 0.0048. \tag{14}$$

The value corresponds to just 2.1 MHz of BW at the center frequency $f_0 = 436.5$ MHz. Thus, it is expected that the total application bandwidth BW = 3.2 MHz will be covered with a VSWR value higher than 2:1.

5.2 Antenna geometry evolution
The number and arrangement of the peripheral slits along the edges of the CubeSat patch antenna have been influenced by the design strategy of (Notis et al., 2004). The authors used slits of maximum length equalling 380 mil (9.5 mm) for a patch length 1620 mil (40.5 mm); slit depth was 23% of patch length. The slits were 20-mil (0.5-mm) wide, whereas inter-slit distance was 40 mil (1 mm). The starting centre frequency of that study was $f_0^\text{Notis} = 2.36$ GHz. The frequency ratio between the two studies equals 5.4, therefore frequency scaling leads to roughly 2.5-mm wide slits with inter-slit spacing equal to 5.0 mm. The total edge length occupied by the 10 slits in (Notis et al., 2004) was

$$W_\text{total}^{10} = 10 \cdot 20 + 40 \, (10 - 1) \ \text{mil} = 560 \ \text{mil}. \tag{15}$$

Consequently, the portion of the patch edge occupied by the slits is

$$\frac{560}{1620} = \frac{28}{81} \simeq \frac{1}{3},$$

which is a reasonable design choice, since provisions for circular polarization were made in (Notis et al., 2004) as well.

The CubeSat antenna was designed by etching 10 slits on each of the 4 sides of the square patch. The slits have variable width (but equal for all), and also variable length that follows a certain set of values $\{a_1, a_2, a_3, a_4, a_5\}$. To preserve the potential for circular polarization,

slit configuration has been chosen in a way that maintains the two perpendicular symmetry axes (see Fig. 10). This is the reason why there are only 5 length variables in the previous set, instead of 10.

Since the slits have been etched on the periphery of the patch and not, for example, on the ground plane, the most natural way of spatially modulating (tapering) their lengths is the *triangular distribution*. Theoretically, this tapering would force the current to go through the center of the patch, and thus produce an effective physical length

$$L_{\text{eff}} = L_{\text{patch}} \sqrt{2}. \tag{16}$$

Simulations of antenna models using the triangular tapering started out with a 33% total edge coverage. The parametric sweeps indicated that the estimation of (12) was quite correct: the optimal fractional inset depth lies between 0.36 and 0.38. It is obvious from Fig. 10 that the shape of the slits enables us to increase their width, and therefore occupy a larger part on each side of the square; this leads to a greater miniaturization degree. The study indicated that good results are obtained when the slits take over 70–80% of every side. Furthermore, it was discovered that a good compromise between miniaturization and bandwidth is obtained when the ratio of slit width to slit gap is set around unity. Simulations showed beyond any doubt that this ratio affects both f_0 and $Z_{\text{in}}(j\omega)$. Changes in input impedance are critical and must occur in a controlled manner: the CubeSat antenna is electrically small, thus it is rather challenging to tune it ($X_{\text{in}}(j\omega) \neq 0$) and match it ($R_{\text{in}}(j\omega) \ll 50\ \Omega$).

Fig. 10 illustrates in perspective the final antenna geometry; the tall substrate is evident. This particular model, which is just a 2-layer PCB, represents the first completed design stage; it is designated as the *CubeSat Patch Prototype version 1* and abbreviated herein as "CSPP–1". In Section 5.5 and Section 5.6 we will present the second completed design stage, abbreviated herein as "CSPP–2".

The 40 transverse slits along the periphery of the patch increase the distance that current must travel to reach the opposite edge, and thus increase the effective electrical length of the radiator. The increased electrical path, in turn, reduces the physical size of the patch below 100 mm. If the antenna were designed on a foam substrate ($\varepsilon_r \simeq 1.0$), then the nominal patch size would be 344×344 mm^2. This nominal area was initially reduced by 84% due to dielectric loading; the area of the resulting patch was further reduced by 55% due to the slit distribution. Patch side length was reduced by 60% and 33%, respectively. The final antenna converged to dimensions 93×93 mm^2. Its area was reduced 13.7 times; side length was reduced 3.7 times.

Fig. 11 depicts all important dimensions of both the microstrip patch and the substrate. The size of the substrate has been increased beyond 100×100 mm^2 to facilitate the incorporation of the feed network in the same model (i.e., the $\frac{\lambda_g}{4}$ transformer and a small segment of 50-Ω microstrip).

The length of the slits was modulated according to the triangular distribution. Other distributions can also be used, such as binomial, uniform, geometric and cosine-on-pedestal. In fact, (Notis et al., 2004) used the *uniform* distribution. A first estimation on the electrical size of the radiator is $ka = 2\pi \frac{93\sqrt{2}/2}{687.3}$ rad $= 0.60$ rad < 1 rad, and thus the CubeSat antenna is indeed *electrically small*. It remains to be seen how well can such a small cavity-like antenna perform in terms of *gain*, *radiation efficiency*, *quality factor*, *bandwidth* and *half-power beamwidth*.

5.3 CSPP–1 simulation setup

Fig. 12 depicts the spatial discretization (*meshing*) of the model used to design the CSPP–1 antenna. The structure was excited in the time domain by a Gaussian pulse having spectral
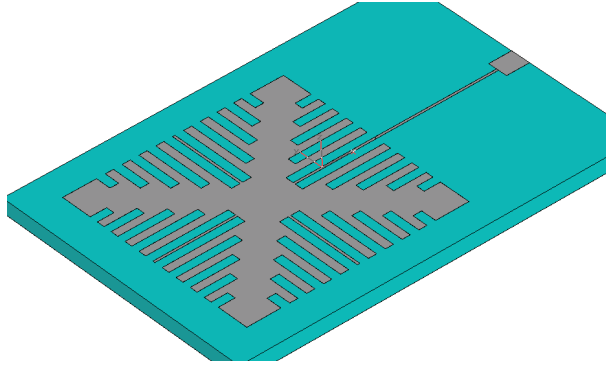
Fig. 10. The square printed CSPP–1 antenna loaded with inductive peripheral slits. The $\lambda_g/4$ transformer and a small segment of 50-Ω microstrip line are also shown.
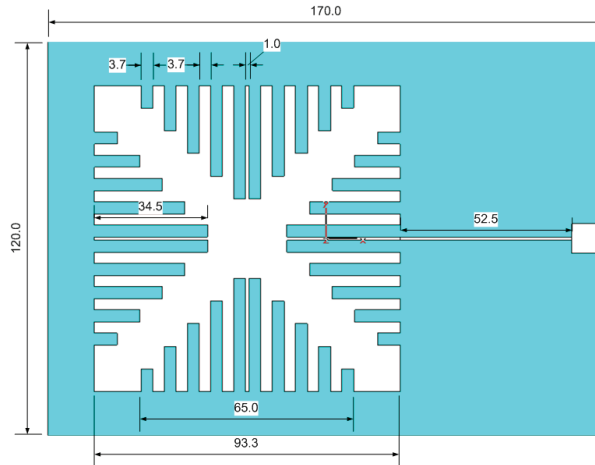

Fig. 11. Converged dimensions of the final model, as they resulted from the optimization process. The circuit is printed on a Rogers RO3006 substrate ($\varepsilon_r = 9.80$, $\tan \delta_e = 0.0020$, $H = 6.4$ mm). All dimensions are in millimetres.

content in the range DC–0.8 GHz. For efficient simulations, a spatially non-uniform (adaptive) grid was designed; maximum allowed grid step was equal to $\lambda_g/36$ at $f_{max} = 0.8$ GHz. The rectangular solvable space surrounding the PCB of the antenna was terminated at a 6-layer Bérenger PML structure (Bérenger, 1994); an antenna cannot be properly simulated unless it is terminated at open-space ("radiating") boundary conditions. Based on our prior experience with the T-Solver, the 6-layer PML provides an excellent accuracy/speed trade-off, in the sense that antenna radiation characteristics converge while simulation time does not increase noticeably (Kakoyiannis et al., 2010; Kakoyiannis & Constantinou, 2010a;b).

Setting the Boundary Conditions (BCs) properly in an antenna simulation is always a major issue. During the CSPP–1 design stages, where high simulation speed was preferred over extreme accuracy, the solvable space was trimmed to half by terminating the area below the substrate at a PEC boundary condition, i.e., $\mathbf{E}_t \equiv 0$. This causes the ground plane of the PCB
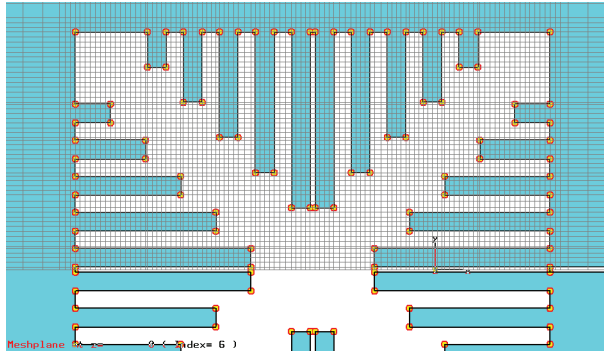
Fig. 12. The grid on which the electromagnetic problem was solved displayed a variable step ranging from 0.3 mm to 4.2 mm. Maximum grid step corresponds to $\lambda_g/36$ (or $\lambda_0/90$) at the maximum frequency $f_{\max} = 0.8$ GHz.

to extend to infinity; now, the mirror backing the patch becomes electrically huge. This is only a practical approximation, since in reality the patch occupies approximately the same area as the ground plane does.

Yet another important BC-related issue is raised by the geometry of the antenna, i.e., the two perpendicular symmetry planes: could electric/magnetic BCs be applied to the model so as to reduce the solvable space to a fraction ($\frac{1}{2}$, $\frac{1}{4}$, $\frac{1}{8}$) of the original? Indeed, after studying the volume field distributions inside the solvable space, one can notice right away that at the boundary of xz-plane the magnetic field $\mathbf{H}(x, y, z, t)$ is normal to the plane ($\mathbf{H}_t \equiv 0$), whereas the electric field $\mathbf{E}(x, y, z, t)$ is tangential. This means that through the xz-plane there is only magnetic flux, and no electric. Therefore, at the xz-plane a magnetic BC (or *magnetic wall*) is applicable; this BC reduces the computational burden to one-half without any loss of accuracy. Fig. 13 illustrates the application of the magnetic wall. Magnetic symmetry was maintained throughout the design stages of the CubeSat antenna. The complexity of the CSPP–1 model was $127 \times 57 \times 39 = 282,321$ cells.

5.4 Numerical electrical performance of the CSPP–1 antenna

After the geometry of the antenna was established, the next (and most important) step towards design closure was to resonate the antenna. Tuning ($X_{\text{in}}(j\omega_0) \approx 0$ Ω) and matching to 50 Ω ($R_{\text{in}}(j\omega_0) \approx 50$ Ω) must be accomplished at the desired frequency without violating any of the other specifications. The result of this procedure is documented through S-parameters and the Smith chart in Fig. 14 and Fig. 15 respectively. The matching/resonance depth is satisfactory ($|S_{11}| \approx -18$ dB), albeit resulting in a narrowband antenna, as expected. It achieves a 2:1 VSWR bandwidth $\text{BW}_{-10\text{dB}} = 2$ MHz, and a 3:1 VSWR bandwidth equal to $\text{BW}_{-6\text{dB}} = 4$ MHz.

The Smith chart shows that the antenna behaves like a capacitor or inductor for most of the frequencies. This is an anticipated result; the antenna is electrically small (this is proven in Section 5.6). Inside its operational bandwidth, a single resonance exists ($dX_{\text{in}}/d\omega > 0$). The swift crossing of the curve through the central area of the chart recounts the small achievable bandwidth.

According to the *cavity model*, which provides an adequate theoretical treatment of microstrip antennas, the dominant component of the electric field is $\mathbf{E}_z = E_z\mathbf{i}_z$. Fig. 16 illustrates the
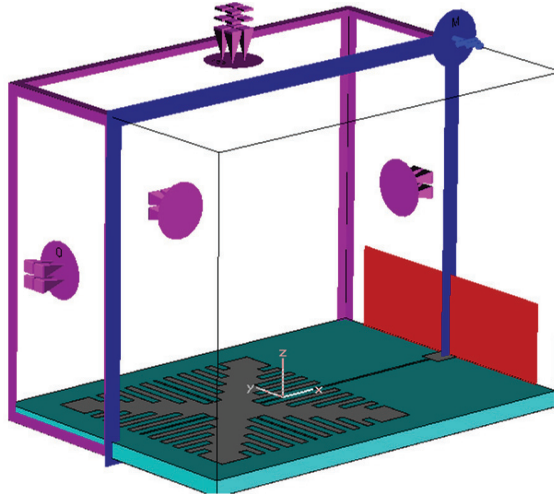
Fig. 13. By applying the magnetic BC $\mathbf{H}_t \equiv 0$ across the xz-plane (blue frame), we get to simulate only the left half of the solvable space, while obtaining equally accurate results. The combination of the magnetic symmetry with the electric BC below the substrate have reduced the computational burden to $1/4$.
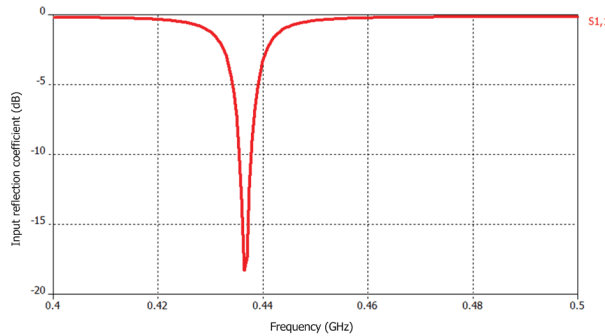

Fig. 14. Resonance and matching at the input of the CSPP–1 antenna given by the magnitude of the input reflection coefficient.

magnitude of the total electric field $\mathbf{E}(x, y, z) = E_x\mathbf{i}_x + E_y\mathbf{i}_y + E_z\mathbf{i}_z$ taken at a snapshot when the field is maximum. Notice that the electric field is strongest not only at the two radiating edges, but also along other vertices along the patch; this is due to the presence of the 40 slits. However, as is well-known from theory, the broadside radiation of microstrip antennas does not result from the z-component of the $\mathbf{E}$-field, but from the two tangential components producing the *fringing field* at the radiating edges of the patch. Fig. 17 illustrates a snapshot of the peak magnitude of the tangential electric field $\mathbf{E}_t = \mathbf{E}_x + \mathbf{E}_y$. Notice how the high-$\varepsilon_r$ keeps the fringing fields too close to the patch. This an ominous conjecture in terms of radiation efficiency; the antenna will tend to behave as a resonant cavity with a small radiating leakage.
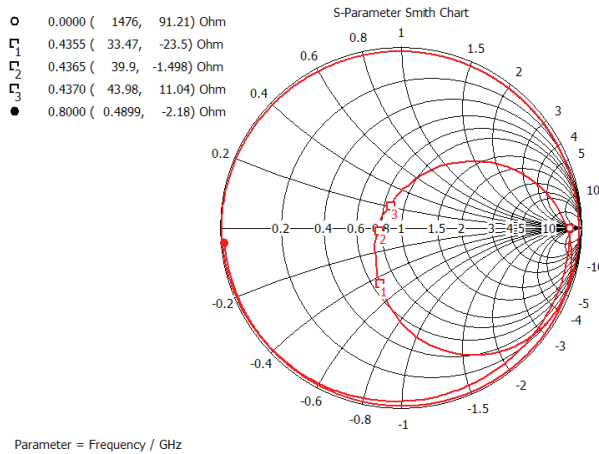
Fig. 15. The CSPP–1 antenna resonates near $f_0 = 436.5$ MHz showing an input resistance $R_{in} \approx 40\,\Omega$.
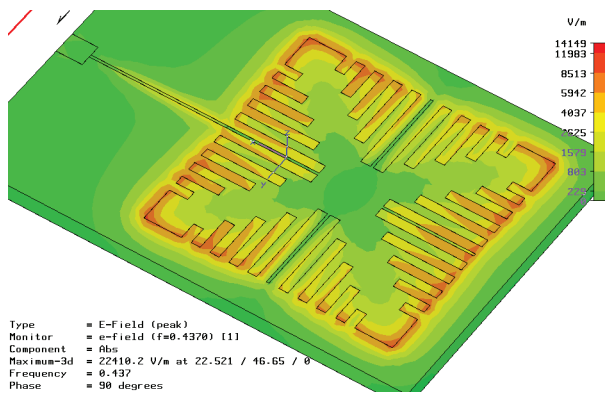

Fig. 16. Maximum magnitude of total **E**-field in the vicinity of the patch. The colour code was set to a logarithmic scale for better resolution.

During all design stages it was very important to check whether the slit distribution would force antenna miniaturization. Visualization of the surface distribution of the current is the way to go; this extremely useful design tool is illustrated by the vector field in Fig. 18. It is evident that the slits do not allow current to travel on a straight line from one radiating edge to the other. Rather, the current moves on a broken line, crossing the center of the patch. Thus, the electrical length of the antenna indeed increases by a factor dependent on maximum slit length.

The study of the CSPP–1 antenna is concluded with the presentation of numerical results pertaining to far-field radiation characteristics. Fig. 19 depicts the three-dimensional (3-D) far-field pattern of the antenna embedded into the model. This pattern was calculated at $f = 437$ MHz and its key aspects are low gain and average radiation efficiency, as it was
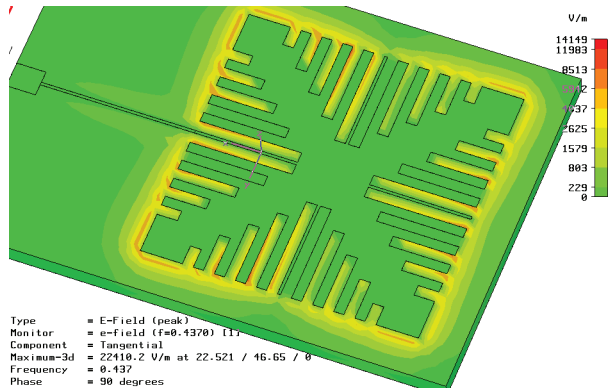
```
Type        = E-Field (peak)
Monitor     = e-field (f=0.4370) [1]
Component   = Tangential
Maximum-3d  = 22410.2 V/m at 22.521 / 46.65 / 0
Frequency   = 0.437
Phase       = 90 degrees
```

Fig. 17. Surface distribution of the peak magnitude of the tangential **E**-field around the patch. The colour code was set to a logarithmic scale for better resolution.
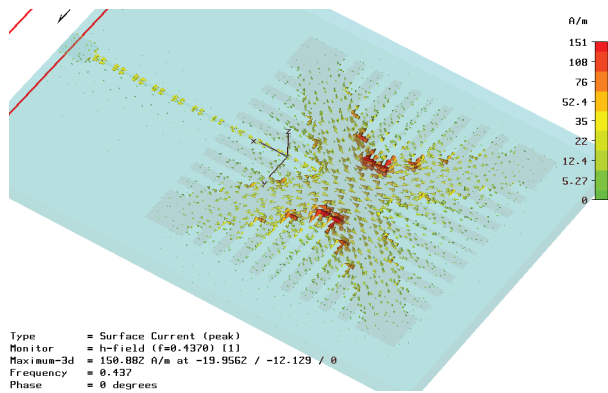


```
Type        = Surface Current (peak)
Monitor     = h-field (f=0.4370) [1]
Maximum-3d  = 150.882 A/m at -19.9562 / -12.129 / 0
Frequency   = 0.437
Phase       = 0 degrees
```

Fig. 18. Visualization of the current distribution on the CSPP–1 patch as a vector field. The color code has been set to logarithmic scale for greater detail.

already predicted:

$$\left.\begin{array}{l} G_{\max} = -1.2 \text{ dBi} \\ n_{\mathrm{rad}} = 0.53 = -2.8 \text{ dB} \end{array}\right\} \tag{17}$$

As a direct consequence of the results in (17), the input resistance of the CSPP–1 antenna $R_{\mathrm{in}}(j\omega) \triangleq \Re\{Z_{\mathrm{in}}(j\omega)\}$ is comprised at resonance by the following two parts:

$$\left.\begin{array}{l} R_{\mathrm{rad}} = 21.2 \text{ } \Omega \\ R_{\mathrm{loss}} = 18.8 \text{ } \Omega \end{array}\right\} \tag{18}$$

The shape of the far-field pattern is anticipated from theory. The abrupt cut is due to the electric boundary condition applied below the substrate; this BC prohibits radiation in the lower semi-space. Therefore, at this design stage there is no information available on the back-lobe. Significant backward radiation is anticipated because of the comparable dimensions of the patch and the ground plane.

A CubeSat is intended to communicate with its ground control within a given frequency range, which the antenna designer must match to the operating bandwidth of the antenna.
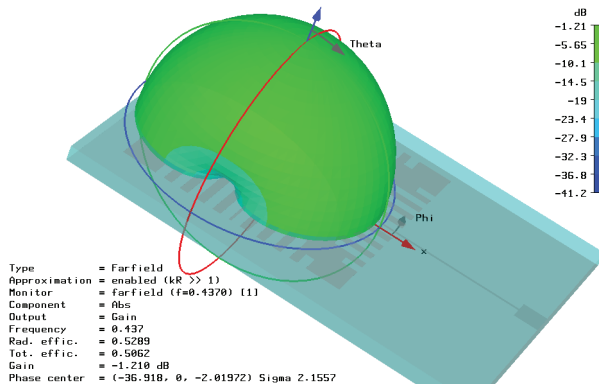
```
Type           = Farfield
Approximation  = enabled (kR >> 1)
Monitor        = farfield (f=0.4370) [1]
Component      = Abs
Output         = Gain
Frequency      = 0.437
Rad. effic.    = 0.5289
Tot. effic.    = 0.5062
Gain           = -1.210 dB
Phase center   = (-36.918, 0, -2.01972) Sigma 2.1557
```

Fig. 19. The gain values of CSPP–1 remain below 0 dBi for all directions in the upper semi-space owing to low radiation efficiency. Radical changes are expected in the more realistic CSPP–2, where the back-lobe will enter the visible region of the pattern.

It would be very useful for the satellite link designer to have information on antenna gain not just for one frequency, but for the whole range of frequencies. To this end, broadband far-field monitoring and recording was facilitated by 17 field monitors uniformly spaced across the 3.2-MHz bandwidth. This recording provided the broadband variation in radiation efficiency n_{rad} (see Fig. 20), total efficiency n_{total} (see Fig. 21) and gain (see Fig. 22).
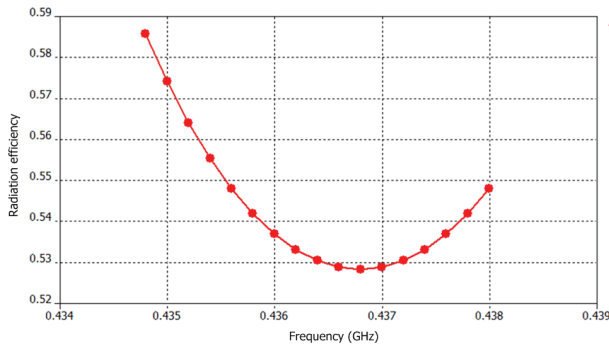
Fig. 20. Broadband variation in the radiation efficiency of the CSPP–1 antenna.

5.5 CSPP–2 simulation setup

The CSPP–2 antenna is a far more realistic model compared to CSPP–1. Two important changes were made to this second prototype: first, the electric boundary condition below the substrate was removed. Thus, all 6 BCs were set to open-space (radiating). The solvable space was terminated at a 6-layer PML, which was separated from every side of the model by $\lambda_c/8$ at $f_c = 0.4$ GHz. Second, a solid PEC rectangular object was mounted right below the substrate, pressing against the ground plane. This PEC object is 100 mm tall, whereas its transverse dimensions are equal to those of the ground plane. It models the chassis of the satellite; it is useful for studying the behaviour of the antenna in what looks like its true operating environment. The realistic CSPP–2 model is depicted in Fig. 23.
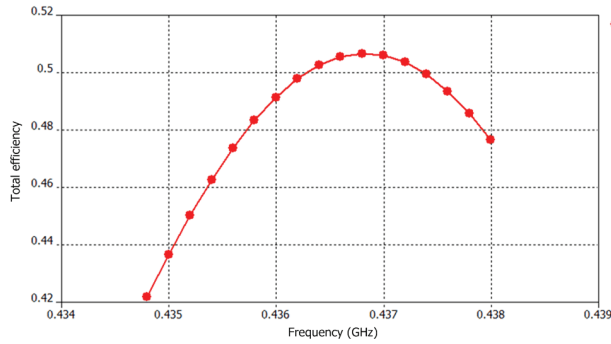
Fig. 21. Broadband variation in the total efficiency of the CSPP–1 antenna.
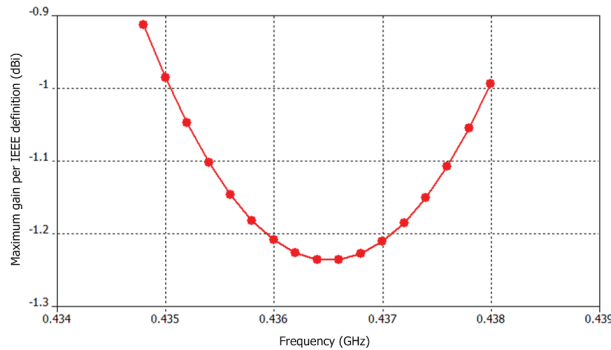

Fig. 22. Broadband variation in the IEEE gain of the CSPP–1 antenna. Peak-to-peak gain flatness equals 0.3 dB.

This was the most complex model that was solved in the framework of this Chapter; the complexity of the solvable space was $143 \times 68 \times 44 = 427,856$ hexahedral cells. Note that the magnetic symmetry across the xz-plane is still applicable. Fig. 24 shows the full solvable space annotated by the 6 boundary conditions.

5.6 Numerical electrical performance of the CSPP–2 antenna

With the planar antenna mounted on the PEC chassis, the first thing that was noticed about its behaviour was that the resonant frequency remained almost constant; it shifted slightly downwards from $f_0 = 436.5$ MHz to $f'_0 = 436.0$ MHz. However, there was a significant change in input *resistance*, which dropped from $R_{\text{in}}(j\omega_0) = 40\ \Omega$ to $R'_{\text{in}}(j\omega'_0) = 23\ \Omega$. The drop can be compensated by reducing the depth of the inset feed, but this is hardly the issue here: this 42% reduction epitomizes the fact that antenna design iterations end only *after* the antenna has been embedded into its working environment, be it a satellite, a cell-phone held by a hand next to a head, a vessel at sea, and so on. If the working environment is not taken into account, even as a very crude model, the system designer will have to settle for an antenna of sub-optimal performance.

The shape of the $|S_{11}|$ curve is essentially preserved, but minimum reflection coefficient increases from -18 dB to -9 dB. The operational bandwidth for a 3:1 VSWR ($S_{11} \leq -6$ dB) remains at $\text{BW}_{-6\text{dB}} = 4$ MHz. Fig. 25 illustrates the variation in $Z_{\text{in}}(j\omega)$ on the Smith chart.
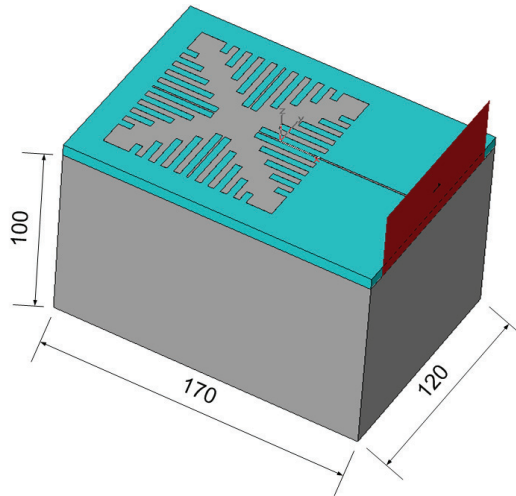
Fig. 23. A 100-mm tall conductive chassis was embedded into the realistic model. The other two sides are longer to fit the size of the substrate. All dimensions are in millimetres.
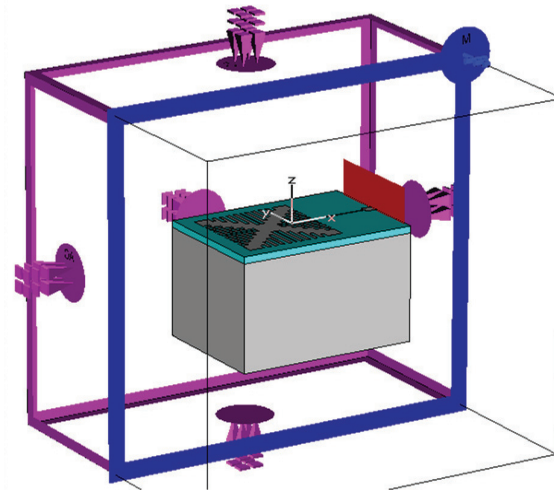

Fig. 24. By applying the magnetic BC $\mathbf{H}_t \equiv 0$ across the xz-plane (blue frame), we get to simulate only the left half of the solvable space, while obtaining equally accurate results. This time, however, there was no electric BC below the substrate.

The far-field pattern of the CSPP–2 model is certainly more intriguing than the textbook-looking one of CSPP–1. The 3-D pattern shown in Fig. 26 confirms the existence of a strong back-lobe, which is created by near-field diffraction on the edges of the ground plane and the PEC chassis. Maximum directivity is $D_{\max} = 4.9$ dBi, but the low efficiency results in a maximum gain $G_{\max} = 0.7$ dBi at $f_0' = 436$ MHz.
The pattern cuts at the principal planes $\phi = 0°$ and $\phi = 90°$ are illustrated in Fig. 27. They too indicate that there is a strong back lobe caused by the patch and the ground plane having
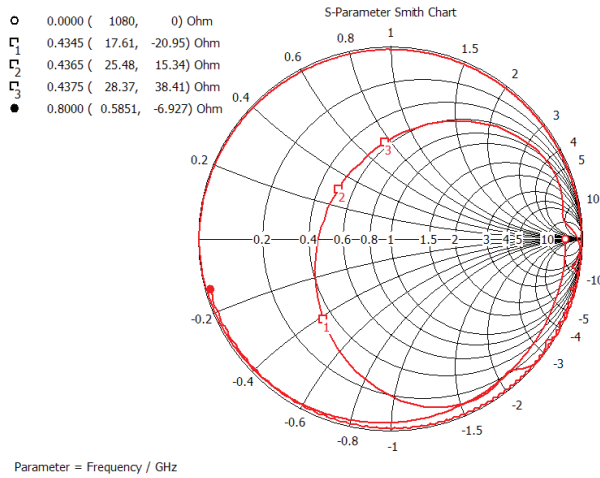
Fig. 25. The CSPP–2 antenna resonates at 436 MHz showing an input resistance $R_{in} \approx 23 \, \Omega$.
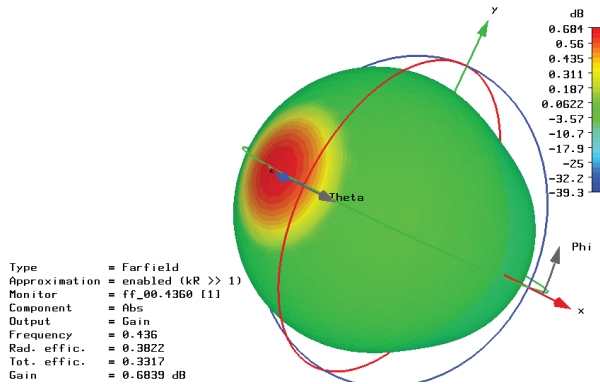

Fig. 26. The 3-D far-field pattern of the CSPP–2 antenna drawn in spherical coordinates. The direction of main-lobe maximum deviates from broadside by $15°$ because of the inset feed, which shifted the phase center by 30 mm along the central axis of the patch.

comparable dimensions. The Front-to-Back Ratio (FBR) of the antenna is FBR = 5 dB, whereas its beamwidth is HPBW = $116°$ at both principal planes. After examining the three patters as a whole, one could suggest that the far-field pattern of this electrically small antenna approximates the isotropic radiator within 5 dB.

Broadband far-field monitoring and recording was also performed for the CSPP–2 model. Recordings of the broadband variation in radiation efficiency n_{rad}, total efficiency n_{total} and gain are depicted in Fig. 28, Fig. 29 and Fig. 30 respectively.

This section is concluded with the calculation of the *electrical sizes* of the two antennas. The electrical size is required for the calculations tabulated in Table 1. The vector SCD in Fig. 31 indicates that the slit distribution works equally well for the CSPP–2 antenna. Therefore, the following calculations apply to both antenna models.
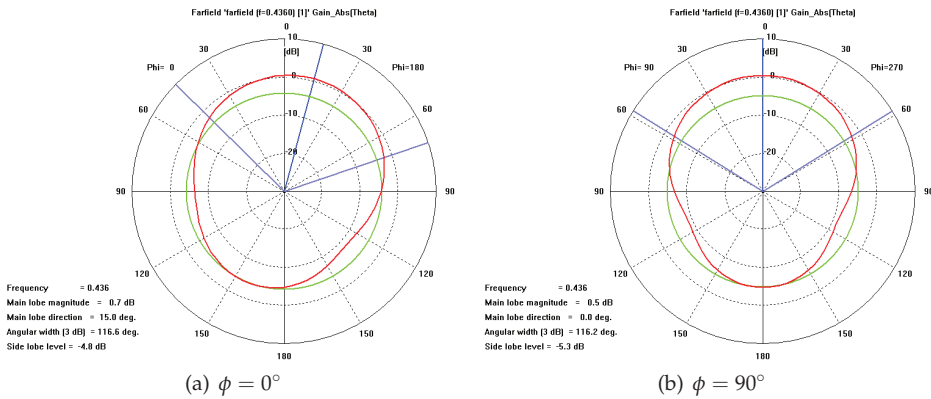
Fig. 27. Pattern cuts at the $\phi = 0°$ and $\phi = 90°$ principal planes. On the latter plane the front-to-back ratio is 0.5 dB higher (FBR = 5.3 dB).
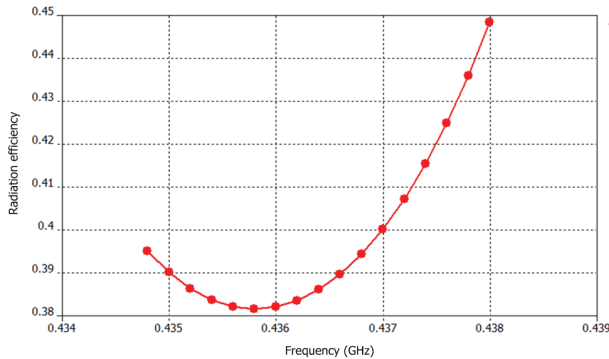

Fig. 28. The radiation efficiency of the CSPP–2 antenna varies between 38–45% throughout the service band of the CubeSat.

First of all, we need to calculate the radius of the *circumscribing sphere*, that is, the thought spherical surface that circumscribes all *radiating parts* of the antenna. To this end, we have used the surface current distribution shown in Fig. 32. According to Sten's theoretical treatment, the radius of the circumscribing sphere should be calculated by placing the centre at the feed point of the planar antenna (Bancroft, 2004; Sten et al., 2001). This holds for printed monopole antennas, which, according to Image Theory, use a parallel ground plane to "mirror" the other half of the antenna that is missing, thus becoming asymmetric dipoles. Obviously, microstrip patch antennas do not form an image, since they are nominally half-wavelength antennas. Therefore, the centre of the sphere was placed at the centre of the square patch. Apart from all the above, the radius must be wide enough to accommodate the whole of the surface current distribution, i.e., the radiating parts of the antenna. Including just the patch may not suffice; currents exist also on the upper face of the ground plane below, and these currents contribute to radiation, too. This SCD is free to extend beyond the limits of the patch (Bancroft, 2004). This phenomenon occurs in CSPP–1 and CSPP–2: the lower SCD extends to the edges of
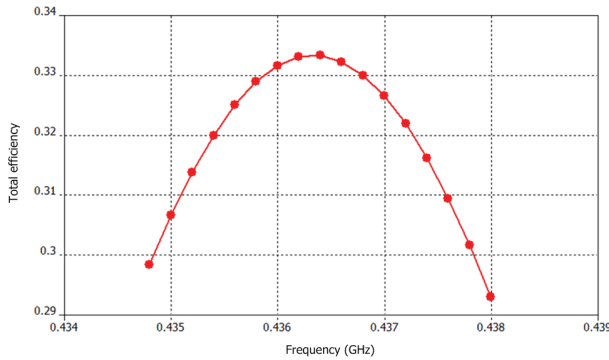
Fig. 29. The total efficiency of the CSPP–2 antenna varies between 29–33% throughout the service band of the CubeSat.
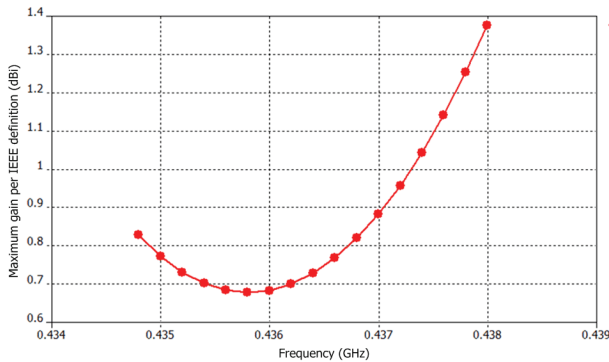

Fig. 30. The maximum gain of the CSPP–2 antenna varies between 0.7–1.4 dB throughout the service band of the CubeSat.

the ground plane. Finally, the radius of the circumscribing sphere is $a = 64.2$ mm, and the resulting electrical size of the antenna is

$$(ka)_{\text{CubeSat}} = 2\pi \frac{64.2}{687.3} \text{ rad} = 0.587 \text{ rad} < 1 \text{ rad}. \tag{19}$$

Therefore, the radiator proposed in this Chapter is indeed an *Electrically Small* Antenna (ESA) (Hansen, 1981).

6. Discussing the results

Table 1 summarizes the electrical performance of the CubeSat antenna. Based on the tabulated data, it is easy to derive the Quality Factor of the antenna from the relation (Yaghjian & Best, 2005)

$$Q = \left(\frac{2}{B}\right) \cdot \left(\frac{S-1}{2\sqrt{S}}\right) \tag{20}$$
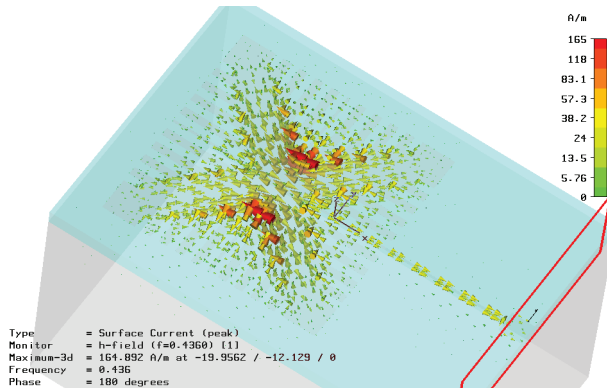
Fig. 31. Visualization of the current distribution on the CSPP–2 patch as a vector field. The color code has been set to logarithmic scale for greater detail.
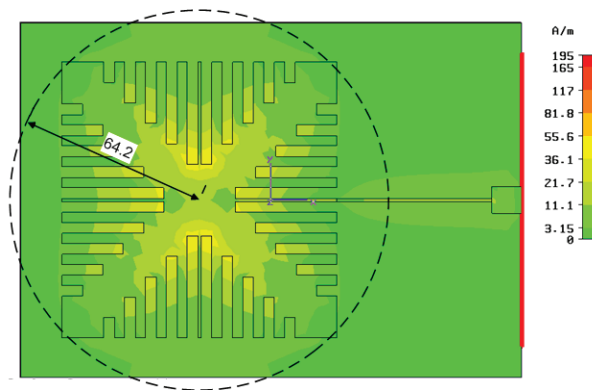

Fig. 32. Definition of the radius of the circumscribing sphere for the CubeSat antenna.

where B is the fractional VSWR bandwidth and S is the corresponding VSWR. Setting $S = 3$, we get $B = 0.0092$, and (20) leads to a loaded Quality Factor

$$Q^{\text{Cube}} = \frac{1}{0.0092} \cdot \frac{3-1}{\sqrt{3}} = 125.5. \tag{21}$$

Another useful expression for calculating the loaded Q of antennas comes from (Pues & Van de Capelle, 1989)

$$Q_{ST} = \frac{1}{B} \sqrt{\frac{(TS-1)(S-T)}{S}} \tag{22}$$

where T is the VSWR level that corresponds to the minimum reflection coefficient. In our case, $\min\{|\Gamma_{\text{in}}(j\omega)|\} = -18$ dB, so the corresponding standing-wave ratio is $S = 1.29$. Substituting these values in (22) we obtain

$$Q_{ST}^{\text{Cube}} = \frac{1}{0.0092} \sqrt{\frac{(1.29 \times 3 - 1)(3 - 1.29)}{3}} = 139 \tag{23}$$

which is 10% higher than the estimation of loaded Q in (21).

Antenna Attribute	Value
Centre frequency, f_0	436.5 MHz
Square patch size, L_{patch}	93.3 mm
3:1 VSWR bandwidth, BW_{-6dB}	4 MHz
Fractional VSWR bandwidth, FBW_V	0.92%
Electrical size, ka	0.587 rad
Quality factor, Q	125.5
Lower bound on Q, $Q_{\ell b}$	2.53
Radiation efficiency at mid-band, n_{rad}	38%
Maximum gain at mid-band, G_{max}^{Cube}	0.7 dBi

Table 1. Overview of the electrical performance of the proposed antenna

The lower bound on Q according to Chu and McLean is calculated by the following equation after substituting the values $n_{rad} = 0.38$ and $ka = 0.587$ rad (Lopez, 2006; Skrivervik et al., 2001; Yaghjian & Best, 2005)

$$Q_{\ell b}^{Cube} = n_{rad} \left[\left(\frac{1}{ka} \right)^3 + \frac{1}{ka} \right] = 2.53. \qquad (24)$$

It has been shown that, as a rule-of-thumb, it is safe to assume that a feasible antenna can achieve a quality factor 75% higher than the lower bound $Q_{\ell b}$ (Lopez, 2006). Assuming that the antenna maintains a constant radiation efficiency and electrical size, then the bandwidth corresponding to a 75% higher Q is equal to

$$BW_{-6dB}^{max} = 113.5 \text{ MHz} \qquad (25)$$

or equivalently,

$$BW_{-10dB}^{max} = 56.8 \text{ MHz}. \qquad (26)$$

From the above we gather that a generic antenna of electrical size $ka = 0.587$ rad could achieve 28 times as much bandwidth as the cavity-like CubeSat patch antenna with its inherently narrow bandwidth.

Similarly, the *upper bound* on *gain* for an antenna of given electrical size ka that also achieves some meaningful operational BW is given by Harrington's equation (Harrington, 1960; Skrivervik et al., 2001)

$$G_{ub}^{Cube} = 10 \log \left[(ka)^2 + 2(ka) \right] = 2.3 \text{ dBi}. \qquad (27)$$

The upper bound on gain was approached by the CubeSat antenna within a margin

$$G_{ub}^{Cube} - G_{max}^{Cube} = 1.6 \text{ dB} \qquad (28)$$

which is very satisfactory. However, in the conclusions of his seminal paper, Harrington notes that none of the concepts described therein holds for *small antennas*; thus the calculation in (27) is not valid, the reason being that small antennas are actually capable of significantly higher gains than the values predicted by the upper bound. But, Harrington's equation can be useful in the ESA case if we mirror the question: given the gain of the small antenna, what would its electrical size be if it were *electrically large*? This introduces the notion of *effective electrical size*, $(ka)_{eff}$. In our case, the effective size turns out to be $(ka)_{eff} = 0.48$ rad, that is,

even smaller than the actual electrical size of the CubeSat antenna due to the low radiation efficiency. As a further example, let us assume that radiation efficiency could climb to 100%. This would produce a new gain value $G_{\text{peak}}^{\text{Cube}} = 4.9$ dBi, and the effective size would then become $(ka)_{\text{eff}} = 1.02$ rad.

6.1 Comparison with existing studies

The first goal of a comparison is to be meaningful; only then will it produce some useful conclusions. The literature review in Section 3 surveyed over fourty different antenna topologies, which spanned four different functions (see Section 2) and six different frequency bands. The statistics of the examined set reveal that 7% of antennas operated in the VHF band; 29% operated in the UHF band; 10% operated in the L-band; 37% operated in the S-band; 2% operated in the C-band; and 15% operated in the X-band. Different frequencies do not pose a problem: fractional bandwidth and electrical size are frequency–normalized quantities, whereas gain is related to directivity, which is determined by the electrical aperture. Hence, an inter-band comparison is still valid. Radiation efficiency is weakly dependent on frequency, so this attribute could also be included in the comparison. However, only (He & Arichandran, 2001) have included details on n_{rad} in their report.

Different functions, on the other hand, can certainly be a problem. GPS/GNSS and TTC subsystems rely on low-gain, broad-beam antennas. Data downlinking and satellite cross-linking is done through medium-/high-gain, directive antenna systems. Increased gain requires a large electrical size, period.[4] Therefore, the electrical performance of the electrically small TTC antenna described herein is compared with the performance of previously reported antennas aimed at GPS/GNSS and TTC subsystems. The comparison is shown in Table 2.[5] The upper part of the Table is reserved for non-planar structures, whereas the lower part tabulates planar ones.

Commenting on the tabulated results, it is first noted that quadrifilar helices (Niow et al., 2009; Rezaei, 2004) are wideband MGAs with clean circular polarization but they are also electrically large structures ($ka > 2$ rad). With proper structure modification and extensive dielectric loading they can be shrunk down to resonant size, that is, the electrical size of the half-wavelength monopole. Bent-wire monopoles (Yousuf et al., 2008) are wideband antennas with reasonable size. Their main drawback is that their performance degrades when mounted on a small satellite.

Turning to the planar antenna regime, the antennas presented by (Mathur et al., 2001) are directly comparable with the CSPP antennas, particularly the UHF antenna. These are electrically small, narrowband antennas as well. Their size exceeds that of the CSPP by 21% and 14% in the UHF and S-band case, respectively. At the other end of the design spectrum, the work by (Muchalski et al., 2004) is a typical example of how suspended, electrically large patches can exhibit quite significant bandwidths. Furthermore, resonant-size patches can produce gains in the range 4–6.5 dBi and bandwidths of a few percent (Gao et al., 2008; Hamrouni et al., 2009; Maqsood et al., 2010). On the other hand, 3-D structures consisting of folded and stacked radiating parts offer moderate bandwidths and gains combined, and can even become electrically small (Lee & Woo, 2008). And last but not least, patch-excited cups are electrically large MGAs offering significant gain values with respect to their size (Zackrisson, 2007). However, in their current form, their size is prohibitive for UHF CubeSat

---

[4] Only compound field antennas threaten to alter this otherwise fundamental relationship, however that topic is outside the scope of and space available in this Chapter.

[5] The FBW cited for (Gao et al., 2008) is aggregate, not instantaneous.

Antenna Configuration	f_0 (GHz)	FBW (%)	G_{max} (dBi)	ka (rad)
(Rezaei, 2004)	2.260	5.4	n/a	2.11
(Yousuf et al., 2008) I	0.370	37.8	n/a	1.41
(Yousuf et al., 2008) II	0.180	32.8	n/a	1.26
(Yousuf et al., 2008) III	0.150	41.8	n/a	1.26
(Niow et al., 2009) initial	2.600	30.8	4.0	2.22
(Niow et al., 2009) Teflon	2.600	15.4	4.0	1.78
(Niow et al., 2009) Macor	2.600	15.4	3.7	1.72
(Mathur et al., 2001) UHF	0.450	1.6	n/a	0.71
(Mathur et al., 2001) S-band	2.260	0.8	4.9	0.67
(Muchalski et al., 2004) centre	2.450	8.2	n/a	2.24
(Muchalski et al., 2004) edge	2.350	8.5	n/a	2.15
(Muchalski et al., 2004) corner	2.275	7.9	n/a	2.08
(Zackrisson, 2007) GPS L2	1.227	n/a	7.4	2.20
(Zackrisson, 2007) GPS L1	1.575	n/a	8.5	2.82
(Zackrisson, 2007) X-band RX	8.000	n/a	8.9	2.63
(Zackrisson, 2007) X-band TX	8.000	n/a	7.5	2.24
(Gao et al., 2008)	2.250	22.2	6.5	1.99
(Lee & Woo, 2008) TX	2.487	6.6	5.3	1.39
(Lee & Woo, 2008) RX	1.610	4.8	2.4	0.90
(Hamrouni et al., 2009) 1	2.400	2.9	n/a	1.62
(Hamrouni et al., 2009) 2	2.400	3.6	n/a	1.62
(Maqsood et al., 2010) L1	1.575	1.0	6.3	1.82
(Maqsood et al., 2010) L2	1.227	0.3	4.0	1.42
This work, CSPP–2	0.437	0.5	0.7	0.59

Table 2. Comparison of electrical performance among GPS/GNSS/TTC antennas

missions since it is 3.7–4.8 times larger than the size of the CSPP, which fits marginally on the wall of the spacecraft.

Judging by the sizes listed in the right-most column of Table 2, it becomes immediately clear that antenna miniaturization techniques are utterly relevant to modern small satellites.

7. Conclusions and further research

Modern small satellites are designed and developed at costs and timescales that are revolutionizing the satellite industry. These satellites range in size from 10–100 kg down to less than 100 g, take a year or less to develop and launch, and have individual costs ranging from a few million dollars to under $1,000. They achieve sophisticated functionality by utilizing state-of-the-art commercial off-the-shelf components, which are initially developed for terrestrial applications and later adapted to space applications. Advances in low-power microelectronics and digital signal processing are turning satellites smaller, smarter, faster and cheaper (Gao et al., 2009). The history and framework of small satellites were described in Section 1. Within this framework, Section 2 defined the objectives of this Chapter. Section 3 presented an overview of the status of antennas for such small satellites. Work from many research groups around the world has been included. Although the focus was on planar antenna structures, linear and 3-D antennas were also described.

From the analysis, design procedure and results presented in sections 4, 5 and 6, it is clear that designing a 1U CubeSat antenna at the lower end of the UHF spectrum is a challenging task. There are too many constraints, and the designer cannot enhance one aspect of the antenna without seriously compromising another. The specifications lead inevitably to the implementation of an *electrically small* antenna. The antenna must be made so small that its performance suffers in every aspect. From the designer's point-of-view, the feasibility of implementing an electrically large antenna ($ka > 2$ rad), or even a resonant-size antenna ($1 < ka < 2$ rad), would be highly desirable. Such a radiator would have significantly better performance, and it would aid the link budget with its higher gain. The need for higher gain becomes evident if we consider that the path loss for a CubeSat is about 140 dB.

However, since the outer dimensions of CubeSats are fixed, there is really no point in suggesting modifications; the system would fall outside protocol specifications. The designer could suggest using more than one faces of the cube. This scenario also comes to no avail, since there can be only one *Earth Facing Facet*. Therefore, it seems that the only way to get a better antenna would be to switch to higher frequencies and, more specifically, at least double the frequency (0.9 GHz). The higher frequency offers many design advantages and one very important drawback: path loss increases by 6 dB. Will the new antenna system be able to compensate this loss, so that it becomes worthy of the time required for the re-design?

The answer is that there is indeed potential to cover the extra loss. Starting with 40×40 mm^2 square patches over a 100×100 mm^2 ground plane, we get the choice of increasing the patch width and switch to rectangular patches, which show better input matching, higher total efficiency and broader bandwidth. Moreover, two rectangular patches forming a two-element linear broadside array can be fed in-phase with a corporate feeding network. Nonetheless, even if the orthogonal patches maintain the double orthogonal symmetry, axial ratio will shift from unity and the purity of circular polarization will degrade.

Another interesting topic for further research is to study different length distributions (tapering) for the peripheral slits. The triangular tapering seemed like a natural choice, but there are other options, e.g. binomial, cosine-on-pedestal, etc. It would be interesting to investigate how the other distributions perform in terms of the size-bandwidth trade-off, because each distribution will affect L_{eff} and $Z_{in}(j\omega)$ differently.

Finally, regardless of the frequency of operation of the CubeSat antenna, there is great interest in studying applicable techniques for broadband microstrip antennas. One such technique is the etching of slots on the surface of the patch that are shaped after the letters "U" and "E". This technique is presented in the most elegant way by (Weigand et al., 2003) and (Shafai, 2007). Again, such broadbanding techniques destroy the double orthogonal symmetry of the patch, and hence do not provide for clean circular polarization.

8. Acknowledgements

9. References

Arnieri, E.; Boccia, L.; Amendola, G. & Di Massa, G. (2004). A high gain antenna for small satellite missions, *IEEE Antennas and Propagation Society Int'l Symposium, 2004*, Vol. 2, pp. 1587–1590, Jun. 2004

Arnieri, E.; Boccia, L.; Amendola, G. & Di Massa, G. (2007). A compact high gain antenna for small satellite applications. *IEEE Transactions on Antennas and Propagation*, Vol. 55, No. 2, pp. 277–282, Feb. 2007

Bahl, I. & Bhartia, P. (2003). *Microwave Solid State Circuit Design*, Wiley-Interscience, ISBN 0471207551, Hoboken, New Jersey

Bancroft, R. (2004). *Fundamental dimension limits of antennas: Ensuring proper antenna dimensions in mobile device designs*. Centurion Wireless Technologies, Westminster, Colorado [Online]. Available: http://www.xertex.com/home/pdf/wp_dimension_limits.pdf (accessed September 30, 2010)

Bérenger, J.P. (1994). A perfectly matched layer for the absorption of electromagnetic waves. *Journal of Computational Physics*, Vol. 114, No. 2, pp. 185–200, Feb. 1994

CubeSat programme & community official website [Online]. Available: www.cubesat.org/ (accessed June 11, 2010)

Dabrowski, M.J. (2005). *The design of a software system for a small space satellite*. M.Sc. thesis, Graduate College, Univ. of Illinois at Urbana-Champaign, Urbana, IL, 2005

Fujishige, T.S.; Ohta, A.T.; Tamamoto, M.A.; Goshi, D.S.; Murakami, B.T.; Akagi, J.M. & Shiroma, W.A. (2002). Active antennas for CubeSat applications, *Proceedings of the 16th AIAA/USU Annual Small Satellites Conference*, paper SSC02-V-2, Utah State University, Logan, USA, Aug. 2002

Galysh, I.; Doherty, K.; McGuire, J.; Heidt, H.; Niemi, D. & Dutchover, G. (2000). *CubeSat: Developing a standard bus for picosatellites*. The StenSat Group, 9512 Rockport Rd, Vienna, VA 22180 [Online]. Available: http://cubesat.net/images/Papers/stensat_hist.pdf (accessed September 30, 2010)

Galván, J. & Colantonio, D. (2009). Low back radiation compact antenna for data downlink in LEO satellites, *Proceedings of the 2009 SBMO/IEEE MTT-S Int'l Microwave and Optoelectronics Conference (IMOC'09)*, pp. 816–820, Belem, Brazil, Nov. 2009

Gao, S.; Brenchley, M.; Unwin, M.; Underwood, C.I.; Clark, K.; Maynard, K.; Boland, L. & Sweeting, M.N. (2008). Antennas for small satellites, *Proceedings of the 2008 Loughborough Antennas and Propagation Conference*, pp. 66–69, Loughborough, UK, Mar. 2008

Gao, S.; Clark, K.; Unwin, M.; Zackrisson, J.; Shiroma, W.A.; Akagi, J.M.; Maynard, K.; Garner, P.; Boccia, L.; Amendola, G.; Massa, G.; Underwood, C.; Brenchley, M.; Pointer, M. & Sweeting, M.N. (2009). Antennas for modern small satellites. *IEEE Antennas and Propagation Magazine*, Vol. 51, No. 4, pp. 40–56, Aug. 2009

Gustrau, F. & Manteuffel, D. (2006). *EM Modeling of Antennas and RF Components for Wireless Communications Systems*, Springer-Verlag, ISBN 3540286144, Berlin, Germany

Hadj Abderrahmane, L.; Benyettou, M.; & Sweeting, M.N. (2006). An S band antenna system used for communication on earth observation microsatellite, *Proceedings of the 2006 IEEE Aerospace Conference*, Big Sky, Montana, USA, Mar. 2006, doi: 10.1109/AERO.2006.1655813

Hamrouni, C.; Neji, B.; Alimi, A.M. & Schilling, K. (2009). Design and prototype of a flight microstrip antennas for the Pico satellite ERPSat-1, *Proceedings 4th Int'l Conf. Recent Advances in Space Technologies*, pp. 750–755, Constantinople, Turkey, Jun. 2009

Hansen, R.C. (1981). Fundamental limitations in antennas. *Proceedings of the IEEE*, Vol. 69, No. 2, pp. 170–182, Feb. 1981

Harrington, R.F. (1960). Effect of antenna size on gain, bandwidth, and efficiency. *J. Res. Nat. Bur. Stand*, Vol. 64, No. 1, pp. 1–12, Jan. 1960

He, Y. & Arichandran, K. (2001). The design of X band dual feed aperture coupled patch antenna for microsatellites, *Proceedings of the IEEE 2001 Int'l Geoscience and Remote Sensing Symposium (IGARSS '01)*, vol. 6, pp. 2784–2786, Sydney, Australia, 2001

Heidt, H.; Puig-Suari, J.; Moore, A.S.; Nakasuka, S. & Twiggs, R.J. (2000). CubeSat: A new generation of picosatellite for education and industry low-cost space experimentation, *Proceedings of the 12th AIAA/USU Annual Small Satellites Conference*, paper SSC00-V-5, Utah State University, Logan, USA, Aug. 2000

Hunyadi, G.; Klumpar, D.M.; Jepsen, S.; Larsen, B. & Obland, M. (2002). A commercial off the shelf (COTS) packet communications subsystem for the Montana EaRth-Orbiting Pico-Explorer (MEROPE) CubeSat, *Proceedings of the 2002 IEEE Aerospace Conference*, Vol. 1, pp. 473–478, Big Sky, Montana, USA, Mar. 2002

Idzkowski, B.; Kalka, T.; Linowski, J.; Preisner, M.; Plywacz, G. & Kabacik, P. (2004). The optimization of communication link performance in scientific minisatellites, *Proceedings of the 15th International Conference on Microwaves, Radar and Wireless Communications (MIKON-2004)*, Vol. 3, pp. 997–1000, Warzaw, Poland, May 2004

Kakoyiannis, C.G. & Constantinou, P. (2008). A compact microstrip antenna with tapered peripheral slits for CubeSat RF Payloads at 436MHz: Miniaturization techniques, design & numerical results, *Proceedings of the IEEE International Workshop on Satellite and Space Communications (IWSSC 2008)*, pp. 255–259, Toulouse, France, Oct. 2008

Kakoyiannis, C.G.; Kyrligkitsi, A. & Constantinou, P. (2010). Bandwidth enhancement, radiation properties and ground-dependent response of slotted antennas integrated into wireless sensors. *IET Microwaves, Antennas & Propagation*, Vol. 4, No. 5, pp. 609–628, May 2010

Kakoyiannis, C.G. & Constantinou, P. (2010a). Radiation properties and ground-dependent response of compact printed sinusoidal antennas and arrays. *IET Microwaves, Antennas & Propagation*, Vol. 4, No. 5, pp. 629–642, May 2010

Kakoyiannis, C.G. & Constantinou, P. (2010b). Compact printed arrays with embedded coupling mitigation for energy-efficient wireless sensor networking. *International Journal of Antennas and Propagation – special issue "Mutual Coupling in Antenna Arrays"*, Vol. 2010, Article ID 596291, 18 pages, 2010

LaBerteaux, J.; Moesta, J. & Bernard, B. (2007). Cajun advanced picosatellite experiment, *Proceedings of the IEEE/AIAA 26th Digital Avionics Systems Conference (DASC'07)*, pp. 5.E.2-1 – 5.E.2-7, Dallas, TX, USA, Oct. 2007

Lee, H.-R. & Woo, J.-M. (2008). Miniaturized dual band circularly polarization microstrip antenna for satellite communication, *Proceedings of the 8th Int'l Symposium on Antennas, Propagation and EM Theory (ISAPE 2008)*, pp. 294–297, Kunming, China, Nov. 2008

Lopez, A.R. (2006). Fundamental limitations of small antennas: Validation of Wheeler's formulas. *IEEE Antennas and Propagation Magazine*, Vol. 48, No. 4, pp. 28–36, Aug. 2006

Maleszka, T.; Gorski, P. & Kabacik, P. (2007). On omnidirectional coverage with minimum number of circularly polarized patch antennas placed on minisatellites, *Proceedings of the 2007 IEEE Antennas and Propagation International Symposium*, pp. 3037–3040, Honolulu, Hawaii, USA, June 2007

Maqsood, M.; Bhandari, B.; Gao, S.; De Vos Van Steenwijk, R. & Unwin, M. (2010). Dual-band circularly polarized antennas for GNSS remote sensing onboard small satellites, *Proceedings of the 7th Int'l Symposium on Communication Systems Networks and Digital Signal Processing (CSNDSP'10)*, pp. 86–90, Newcastle upon Tyne, UK, Jul. 2010

Marrocco, G.; Mattioni, L.; Potenza, A.; Milani, F.; Giacomini, A. & Sabbadini, M. (2010). Distributed multi-function antenna system for micro- and nano-satellites, *Proceedings 4th European Conf. Antennas and Propagation (EuCAP'10)*, Barcelona, Spain, Apr. 2010

Mathur, R.; Haupt, R. & Swenson, C. (2001). Student antenna design for a nanosatellite, *Proc. 2001 IEEE Aerospace Conf.*, Vol. 7, pp. 3683–3688, Big Sky, Montana, USA, Mar. 2001

Mizuno, T.J.; Roque, J.D.; Murakami, B.; Yoneshige, L.; Shiroma, G.; Miyamoto, R. & Shiroma, W.A. (2005). Antennas for distributed nanosatellite networks, *Proceedings of the IEEE/ACES Int'l Conference on Wireless Communications and Applied Computational Electromagnetics*, pp. 606–609, Honolulu, Hawaii, USA, Apr. 2005

Moghaddam, E.S.; Aboutorabian, N.; Amiri, S.; Nikmehr, S. & Rezaei, P. (2004). Design and analysis of a dualband antenna for small LEO satellite applications, *Proceedings of the 3rd International Conference on Computational Electromagnetics and Its Applications (ICCEA 2004)*, pp. 228–231, Beijing, China, Nov. 2004

Muchalski, K.; Jagoda, M.; Tomasiak, M.; Gorski, P.; Akonom, A.; Kulig, M.; Barecki, W. & Kabacik, P. (2004). Optimizing TT&C antenna placement on minisatellites, *Proceedings of the 15th International Conference on Microwaves, Radar and Wireless Communications (MIKON-2004)*, Vol. 2, pp. 489–492, Warzaw, Poland, May 2004

Munteanu, I.; Timm, M. & Weiland, T. (2010). It's about time. *IEEE Microwave Magazine*, Vol. 11, No. 2, pp. 60–69, April 2010

Niow, C.H.; Mouthaan, K.; Coetzee, J.C. & Hui, H.T. (2009). Design of a small size dielectric loaded helical antenna for satellite communications, *Proceedings of the Asia Pacific Microwave Conference (APMC 2009)*, pp. 48–51, Singapore, Dec. 2009

Nohmi, M.; Oi, K.; Takuma, S. & Ogawa, M. (2010). Solar paddle antenna mounted on pico-satellite "KUKAI" for amateur radio communication, *Proceedings of the Second International Conference on Advances in Satellite and Space Communications (SPACOMM'10)*, pp. 31–36, Athens, Greece, Jun. 2010

Notis, D.T.; Liakou, P.C. & Chrissoulidis, D.P. (2004). Dual polarized microstrip patch antenna, reduced in size by use of peripheral slits, *Proceedings of the 34th European Microwave Conference*, Vol. 1, pp. 125-128, Amsterdam, Netherlands, Oct. 2004

Pues, H.F. & Van de Capelle, A.R. (1989). An impedance-matching technique for increasing the bandwidth of microstrip antennas. *IEEE Transactions on Antennas and Propagation*, Vol. 37, No. 11, pp. 1345–1354, Nov. 1989

Puig-Suari, J.; Turner, C.; & Ahlgren, W. (2001). Development of the standard CubeSat deployer and a CubeSat class picosatellite, *Proceedings of the 2001 IEEE Aerospace Conference*, Vol. 1, pp. 347–353, Big Sky, Montana, USA, Mar. 2001

Rezaei, P. (2004). Design of quadrifilar helical antenna for use on small satellites, *2004 IEEE Antennas and Propagation Society Int'l Symposium Digest*, Vol. 3, pp. 2895–2898, Monterey, CA, USA, Jun. 2004

Row, J.-S.; Yeh, S.-H. & Wong, K.-L. (2000). Compact dual-polarized microstrip antennas. *Microwave and Optical Technology Letters*, Vol. 27, No. 4, pp. 284–287, Nov. 2000

Schaffner, J.A. & Puig-Suari, J. (2002). The electronic system design, analysis, integration, and construction of the Cal Poly State University CP1 CubeSat, *Proceedings of the 16th AIAA/USU Annual Small Satellites Conference*, Utah State University, Logan, USA, Aug. 2002 [Online]. Available: polysat.calpoly.edu/PublishedPapers/JakeSchaffner_srproj.pdf (accessed September 30, 2010)

Shafai, L. (2007). Wideband microstrip antennas, In: *Antenna Engineering Handbook, 4th ed.*, Volakis, J.L. (Ed.), Chapter 16, pp. 16.27–16.42, McGraw-Hill, New York

Skrivervik, A.K.; Zürcher, J.-F.; Staub, O. & Mosig, J.R. (2001). PCS antenna design: The challenge of miniaturization. *IEEE Antennas and Propagation Magazine*, Vol. 43, No. 4, pp. 12–27, Aug. 2001

Sten, J.C.-E.; Hujanen, A. & Koivisto, P.K. (2001). Quality factor of an electrically small antenna radiating close to a conducting plane. *IEEE Transactions on Antennas and Propagation*, Vol. 49, No. 5, pp. 829–837, May 2001

Stutzman, W.L. & Thiele, G.A. (1998). *Antenna Theory and Design, 2nd ed.*, Wiley, ISBN 0471025909, New York, USA

Tamamoto, M.A. & Shiroma, W.A. (2002). Active antennas and UHF antennas for CubeSat applications, [Online]. Available: www.spacegrant.hawaii.edu/reports/12_FA02-SP03/tamamoto.pdf (accessed September 30, 2010)

Tanaka, M.; Suzuki, R.; Suzuki, Y. & Araki, K. (1994). Microstrip antenna with solar cells for microsatellites, *1994 Antennas and Propagation Society Int'l Symposium Digest*, Vol. 2, pp. 786–789, Seattle, WA, USA, Jun. 1994

Vasylchenko, A.; Schols, Y.; De Raedt, W. & Vandenbosch, G.A.E. (2007a). Challenges in full wave electromagnetic simulation of very compact planar antennas, *Proc. 2nd European Conf. Antennas Propag. (EuCAP 2007)*, pp. 1–6, Edinburgh, UK, Nov. 2007

Vasylchenko, A.; Schols, Y.; De Raedt, W. & Vandenbosch, G.A.E. (2007b). A Benchmarking of six software packages for full-wave analysis of microstrip antennas, *Proc. 2nd European Conf. Antennas Propag. (EuCAP 2007)*, pp. 1–6, Edinburgh, UK, Nov. 2007

Weigand, S.; Huff, G.H.; Pan, K.H.; & Bernhard, J.T. (2003). Analysis and design of broad-band single-layer rectangular U-slot microstrip patch antennas. *IEEE Transactions on Antennas and Propagation*, Vol. 51, No. 3, pp. 457–468, Mar. 2003

Weiland, T.; Timm, M. & Munteanu, I. (2008). A practical guide to 3-D simulation. *IEEE Microwave Magazine*, Vol. 9, No. 6, pp. 62–75, Dec. 2008

Wettergren, J.; Ingvarson, P. & Zackrisson, J. (2009). Data-link antennas for moon-crashing probes, *Proceedings of the Third European Conference on Antennas and Propagation (EuCAP 2009)*, pp. 1891–1895, Berlin, Germany, Mar. 2009

Wikipedia contributors (2010a). CubeSat. *Wikipedia, The Free Encyclopedia*, http://en.wikipedia.org/wiki/Cubesat (accessed June 11, 2010)

Wikipedia contributors (2010b). Miniaturized satellite. *Wikipedia, The Free Encyclopedia*, http://en.wikipedia.org/wiki/Miniaturized_satellite (accessed June 11, 2010)

Wikipedia contributors (2010c). List of CubeSats. *Wikipedia, The Free Encyclopedia*, http://en.wikipedia.org/wiki/List_of_CubeSats (accessed June 11, 2010)

Wincza, K.; Osys, M.; Dudzinski, L. & Kabacik, P. (2004). Lightweight low gain microstrip antennas for use in minisatellites, *Proceedings of the 15th International Conference on*

Microwaves, Radar and Wireless Communications (MIKON-2004), Vol. 1, pp. 314–317, Warzaw, Poland, May 2004

Wong, K.L. & Hsu, W.-H. (2001). A broad-band rectangular patch antenna with a pair of wide slits. *IEEE Transactions on Antennas and Propagation*, Vol. 49, No. 9, pp. 1345–1347, Sept. 2001

Xiao, S.; Wang, B.-Z.; Shao, Z.; Zhou, M.-T. & Fujise, M. (2005). Bandwidth-enhancing ultralow-profile compact patch antenna. *IEEE Transactions on Antennas and Propagation*, Vol. 53, No. 11, pp. 3443–3447, Nov. 2005

Xiao, S.; Shao, Z.; Wang, B.-Z.; Zhou, M.-T. & Fujise, M. (2006). Design of low-profile microstrip antenna with enhanced bandwidth and reduced size. *IEEE Transactions on Antennas and Propagation*, Vol. 54, No. 5, pp. 1594–1599, May 2006

Yaghjian, A.D. & Best, S.R. (2005). Impedance, bandwidth, and Q of antennas. *IEEE Transactions on Antennas and Propagation*, Vol. 53, No. 4, pp. 1298–1324, April 2005

Yousuf, H.J.; Haider, M.M.; Siddique, M.K. & Amin, M. (2008). Analysis of G-shape antennas mounted on a CUBESAT, *Proceedings of the 2nd Int'l Conference on Advances in Space Technologies*, Vol. 2, pp. 28–32, Islamabad, Pakistan, Nov. 2008

Zackrisson, J. (2007). Wide coverage antennas, *Proc. 21st AIAA/USU Annual Conf. Small Satellites*, paper no. SSC07-XIII-7, Utah State University, Logan, USA, Aug. 2007

Zhang, X.-X. & Yang, F. (1998). Study of a slit cut on a microstrip antenna and its applications. *Microwave and Optical Technology Letters*, Vol. 18, No. 4, pp. 297–300, July 1998